



HAL
open science

The Origin of Felsic Intrusions Within the Mantle Section of the Samail Ophiolite: Geochemical Evidence for Three Distinct Mixing and Fractionation Trends

Matthew Rioux, Mathieu Benoit, Isma Amri, Georges Ceuleneer, Joshua Garber, Michael Searle, Kayla Leal

► To cite this version:

Matthew Rioux, Mathieu Benoit, Isma Amri, Georges Ceuleneer, Joshua Garber, et al.. The Origin of Felsic Intrusions Within the Mantle Section of the Samail Ophiolite: Geochemical Evidence for Three Distinct Mixing and Fractionation Trends. *Journal of Geophysical Research : Solid Earth*, 2021, 126 (5), 10.1029/2020JB020760 . hal-03761509

HAL Id: hal-03761509

<https://hal.science/hal-03761509>

Submitted on 26 Aug 2022

HAL is a multi-disciplinary open access archive for the deposit and dissemination of scientific research documents, whether they are published or not. The documents may come from teaching and research institutions in France or abroad, or from public or private research centers.

L'archive ouverte pluridisciplinaire **HAL**, est destinée au dépôt et à la diffusion de documents scientifiques de niveau recherche, publiés ou non, émanant des établissements d'enseignement et de recherche français ou étrangers, des laboratoires publics ou privés.

Copyright

JGR Solid Earth

RESEARCH ARTICLE

10.1029/2020JB020760

Special Section:

Ophiolites and Oceanic Lithosphere, with a focus on the Samail ophiolite in Oman

This article is a companion to Rioux et al. (2021), <https://doi.org/10.1029/2020JB020758>.

Key Points:

- Felsic dikes and sills with epsilon Nd of -7.8 to $+7.8$ intruded the shallow mantle in the Samail ophiolite
- Combined whole rock major element, trace element, and isotopic data define three distinct mixing and fractionation trends
- Most dikes formed by sediment and amphibolite melting on underthrust oceanic lithosphere at $P \leq 1.4$ GPa and $T \geq 700$ – 750°C

Supporting Information:

Supporting Information may be found in the online version of this article.

Correspondence to:

M. Rioux,
rioux@eri.ucsb.edu




Citation:

Rioux, M., Benoit, M., Amri, I., Ceuleneer, G., Garber, J. M., Searle, M., & Leal, K. (2021). The origin of felsic intrusions within the mantle section of the Samail ophiolite: Geochemical evidence for three distinct mixing and fractionation trends. *Journal of Geophysical Research: Solid Earth*, 126, e2020JB020760. <https://doi.org/10.1029/2020JB020760>

Received 11 AUG 2020
 Accepted 25 JAN 2021

© 2021. American Geophysical Union.
 All Rights Reserved.

The Origin of Felsic Intrusions Within the Mantle Section of the Samail Ophiolite: Geochemical Evidence for Three Distinct Mixing and Fractionation Trends

Matthew Rioux^{1,2} , Mathieu Benoit³, Isma Amri⁴, Georges Ceuleneer³, Joshua M. Garber⁵ , Michael Searle⁶ , and Kayla Leal¹

¹Department of Earth Science, University of California, Santa Barbara, Santa Barbara, CA, USA, ²Earth Research Institute, University of California, Santa Barbara, Santa Barbara, CA, USA, ³Centre National de la Recherche Scientifique, Observatoire Midi-Pyrénées, Toulouse, France, ⁴Département de Géologie, Faculté des Sciences, Université Abdelmalek Essaadi, Tétouan, Morocco, ⁵Department of Geosciences, The Pennsylvania State University, University Park, PA, USA, ⁶Department of Earth Sciences, University of Oxford, Oxford, UK

Abstract An isotopically diverse suite of felsic dikes, sills, and plugs ($\epsilon_{\text{Nd}}(t) = -7.8$ to $+7.8$) intrude the uppermost mantle and lower crust in the Samail ophiolite in Oman and the United Arab Emirates (UAE). These features have been interpreted to represent amphibolite and metasediment melts from an underthrust sheet of oceanic lithosphere. As such, the intrusions provide a record of melting of oceanic crust and sediment at depth, with implications for mass transfer from the down-going plate in young, hot subduction settings. Several studies have used geochemical data to constrain the magmatic sources of the dikes; here we build on this previous work using integrated whole rock major element, trace element and Nd isotopic data from a more geographically extensive suite of dikes. New and existing data suggest the felsic intrusions preserved within mantle peridotites in the Oman portion of the ophiolite were generated by three distinct mixing and fractionation trends: (1) three-component mixing between sediment melt, amphibolite melt and a mantle component; (2) two component mixing between amphibolite and sediment melts, with little mantle contribution; and (3) fractional crystallization of depleted, mantle derived magmas, likely related to the ophiolite V2 volcanic series. Combined geochemical and pseudosection modeling suggest that amphibolite melting occurred at $P \leq 1.4$ GPa (~ 40 – 45 km) and $T \geq 700$ – 750°C . Felsic intrusions in the mantle section in the UAE, including garnet-andalusite-cordierite leucogranites, follow similar mixing trends, but crystallized ~ 0.9 – 4.0 Ma after the Oman intrusions.

1. Introduction

The Samail (Oman-United Arab Emirates [UAE]) ophiolite exposes an extensive section of Late Cretaceous oceanic lithosphere. The ophiolite is dominated by ultramafic to mafic rocks, with the exception of small-volume tonalite and trondhjemitic intrusions (“plagiogranites”) in the upper crust (Bailey, 1981; Lippard et al., 1986) and a relatively sparse series of felsic sills, dikes, and plugs that intermittently intrude the uppermost mantle and lower crust along the length of the ophiolite (Adachi & Miyashita, 2003; Amri et al., 1996, 2007; Haase et al., 2015; Lippard et al., 1986; Rollinson, 2009, 2014a, 2015). The upper-crustal tonalite and trondhjemitic intrusions are typically exposed directly below, and intruding into, the base of the sheeted dike complex. They have depleted radiogenic isotope ratios ($\epsilon_{\text{Nd}}(t) \sim +7$ – 8) (Amri et al., 2007; Godard et al., 2006; Haase et al., 2015; McCulloch et al., 1981; Rioux et al., 2012, 2013; Tsuchiya et al., 2013), similar to modern mid-ocean ridges, and geochemical data indicate they are related to either the main phase of ophiolite crust formation at the ridge axis (Geotimes or V1) or the overlying volcanic sequence (Lasail/Alley or V2) (e.g., Adachi & Miyashita, 2003; Haase et al., 2016; MacLeod & Yaouancq, 2000; Pallister & Hopson, 1981). These upper-crustal intrusions have been attributed to crystallization of residual felsic melts derived by fractionation of primitive gabbro (Amri et al., 1996; Pallister & Hopson, 1981) or on-axis anatexis of gabbros or sheeted dikes related to interaction of magmatic and hydrothermal systems (France et al., 2009; Koepke et al., 2004; Nicolas et al., 2008; Rollinson, 2009). Similar rock types are observed at modern slow- and fast-spreading ridges (e.g., Aldiss, 1981; Natland & Dick, 2002; Wilson et al., 2006).

In contrast, the felsic intrusions into the upper mantle and lowermost crust of the ophiolite are geochemically and mineralogically distinct; they are commonly enriched in light rare earth elements (LREE) and

typically have low Nd isotopic ratios ($\epsilon_{\text{Nd}}(t) < 0$; i.e., continent-like), although some have higher positive $\epsilon_{\text{Nd}}(t)$ (Amri et al., 2007; Briquieu et al., 1991; Cox et al., 1999; Haase et al., 2015; Lippard et al., 1986; Rioux et al., 2013). Some of the felsic intrusions in the northern section of the ophiolite within the UAE are more aluminous garnet-, andalusite-, and cordierite-bearing leucogranites. U-Pb zircon dating indicates that the dikes within the Oman portion of the ophiolite intruded toward the end of crustal growth (Rioux et al., 2013, 2021) suggesting they are related to ophiolite formation or emplacement, rather than later obduction onto the continental margin. Based on the geochemical and isotopic data, the intrusions have been interpreted to reflect melting of metasediment and amphibolite on the top of either underthrust oceanic lithosphere (Boudier et al., 1988; Briquieu et al., 1991) or a subducted slab (Haase et al., 2015; Rioux et al., 2013; Rollinson, 2009, 2014a, 2015; Spencer et al., 2017). The dikes are therefore a valuable analog for the melting of oceanic crust and sediment at intermediate pressures and temperatures, which may be an important mass transfer process in young, hot subduction settings (e.g., Maunder et al., 2020; Nikolaeva et al., 2008).

The geochemistry of the felsic intrusions has been the focus of several previous studies (Amri et al., 2007; Briquieu et al., 1991; Cox et al., 1999; Haase et al., 2015; Rollinson, 2009, 2014a, 2015; Spencer et al., 2017). Here, we present new whole-rock major element, trace element, and Nd-isotopic data from intrusions from a broader geographic area than previous studies. Integration of the elemental and isotopic data and the greater geographic extent provides new insight into the source of the felsic intrusions.

2. Geologic Setting

The Samail ophiolite, exposed in Oman and the UAE, is the largest and best studied ophiolite on Earth (Figure 1). It exposes a complete crustal and shallow mantle section, with a general stratigraphy of residual mantle harzburgite, layered gabbro, foliated gabbro, discontinuous upper-level varitextured gabbro and tonalite/trondhjemitic (plagiogranite), basaltic sheeted dikes, and pillow basalts and lava flows (Coleman & Hopson, 1981; Lippard et al., 1986; Nicolas et al., 2000; Pallister & Hopson, 1981). The volcanic sequence in the ophiolite has been divided into the lower Geotimes (V1) and upper Lasail/Alley (V2) series (Alabaster et al., 1982; Ernewein et al., 1988; Lippard et al., 1986; Pearce et al., 1981). Limited sedimentation between the two series suggest that these eruptive events may have been contiguous, with little to no time lapse between them. The V1 series, which is interpreted to reflect the extrusive equivalent to the main portion of the intrusive crust, is chemically similar to mid-ocean ridge basalts (MORB) (Ernewein et al., 1988; Godard et al., 2006), although the lavas follow differentiation trends to lower TiO_2 and higher SiO_2 , and are depleted in Cr, Nb, and Ta relative to typical MORB (MacLeod et al., 2013; Pearce et al., 1981). The overlying V2 (Lasail and Alley) lavas are depleted in fluid-immobile incompatible trace elements (e.g., Nb, Ta, REE, Zr) and enriched in large ion lithophile elements, and have been interpreted to reflect formation in a nascent subduction zone setting (Alabaster et al., 1982; Kusano et al., 2017; Pearce et al., 1981). Lavas in the upper portion of the V2 series have boninitic compositions (Ishikawa et al., 2002; Kusano et al., 2017). A similar dichotomy between MORB and boninitic-andesitic magmatic compositions exists in the population of mafic dikes intruding the mantle section of the ophiolite (Benoit et al., 1999). The two series occupy different portions of the ophiolite, with the MORB dikes increasing in abundance in the southeastern massifs (Benoit et al., 1996; Ceuleneer et al., 1996; Python & Ceuleneer, 2003). Several studies have used field relations and geochemistry to also link intrusive plutonic rocks in the ophiolite crust to the V1 and V2 lavas (e.g., Adachi & Miyashita, 2003; Haase et al., 2016; Tsuchiya et al., 2013; Usui & Yamazaki, 2010), and we refer to these as the V1 and V2 plutonic series in this contribution.

The ophiolite is underlain by a metamorphic sole composed of metabasaltic and metasedimentary lithologies. The highest-grade rocks consist of garnet- and clinopyroxene-bearing amphibolites, which are exposed in a narrow 1–10 m thick layer in direct thrust contact with overlying, highly sheared harzburgite (Cowan et al., 2014; Ghent & Stout, 1981; Hacker & Mosenfelder, 1996; Searle & Cox, 2002; Searle & Malpas, 1980, 1982; Soret et al., 2017). Estimated peak pressures (P) and temperatures (T) of metamorphism for the highest-grade rocks are 770°C–900°C and 1.0–1.3 GPa (Cowan et al., 2014; Gnos, 1998; Hacker & Mosenfelder, 1996; Soret et al., 2017). These are sequentially underlain by lower grade amphibolite- and then greenschist-facies mafic and metasedimentary rocks, defining an inverted metamorphic gradient (Garber et al., 2020; Gnos, 1998; Searle & Malpas, 1980; Soret et al., 2017). These sole units are in turn thrust over

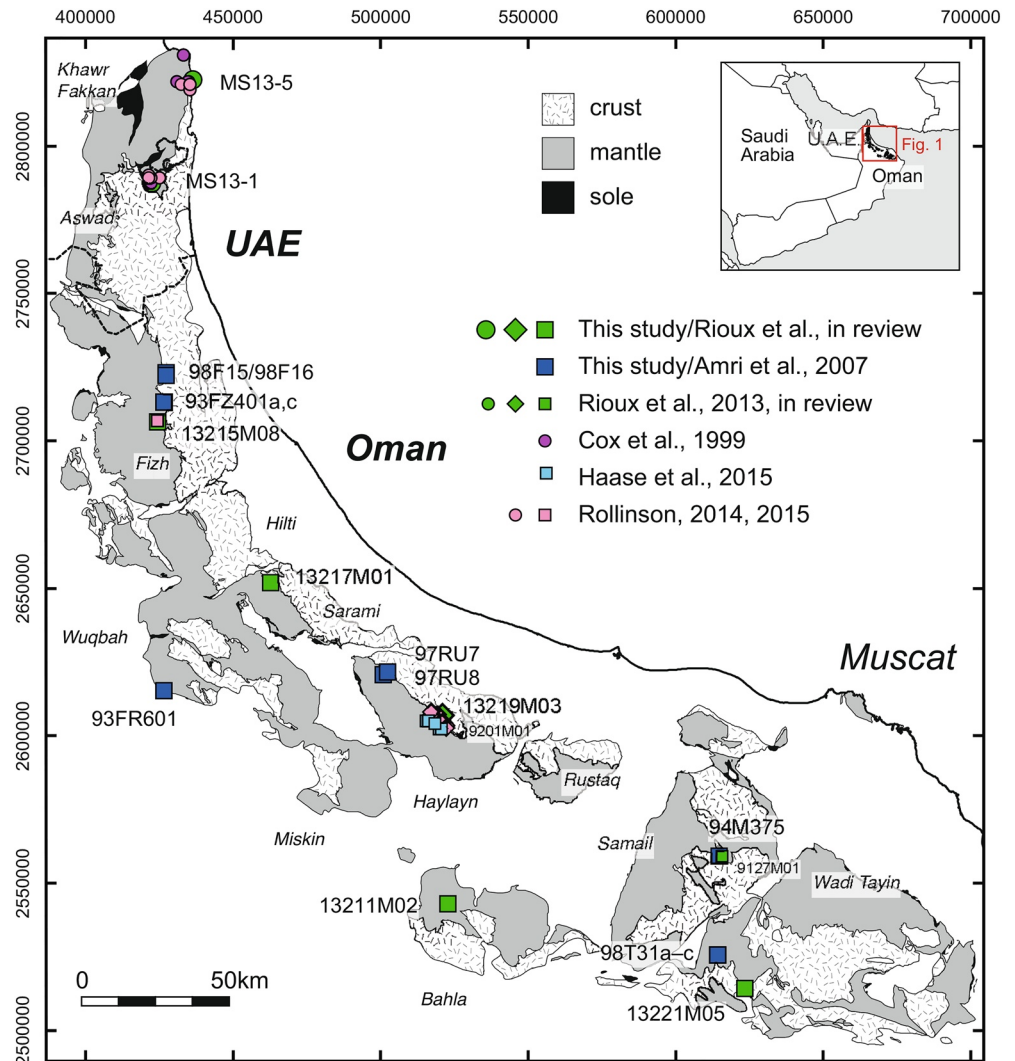


Figure 1. Geologic map of the Samail ophiolite (after Nicolas et al., 2000) showing the location of felsic mantle dikes from this and previous geochemical studies. Larger symbols and text denote samples from this study. Smaller green squares are samples from Rioux et al. (2013) with no whole rock isotope and/or geochemical data. Densely sampled locations from the southern Haylayn massif are offset slightly for clarity. Briquieu et al. (1991) focused on similar areas to the Cox et al. (1999) localities. Massif names are in italics. Map after Nicolas et al. (2000). Plot symbol shapes are consistent with Figures 2, 3, and 5.

low-grade metasedimentary and metavolcanic rocks of the Haybi and Hawasina Formations, which are interpreted as deep-sea sediments, Permian to Triassic limestones, and alkali basaltic seamounts (Searle, 1985; Searle et al., 1980). In the UAE portion of the ophiolite, an out-of-sequence thrust sheet of granulite to upper-amphibolite metasedimentary and minor metabasaltic rocks is preserved within the mantle section at Bani Hamid, with peak P - T conditions of $850 \pm 60^\circ\text{C}$ and 0.63 ± 0.05 GPa (Searle et al., 2015).

The felsic intrusions that are the focus of this study typically occur as ~ 1 – 10 m thick dikes, plugs, and sills that intrude the upper mantle and lowermost crust of the Samail ophiolite, although some intrusions are thicker (e.g., Bahla); for simplicity, we henceforth refer to these intrusions as “felsic mantle dikes”. The dikes are found intermittently along the entire length of the ophiolite (Figure 1). Where present, they often occur in clusters or swarms, but individual swarms occur tens of kilometers apart, with only a few dike localities in each massif. The dikes are generally classified as diorites, tonalites, trondhjemites, and granites with 65–84 wt% SiO_2 . In addition to their unique field context and major element expression, the dikes are isotopically distinct from the rest of the ophiolite. The V1 and V2 magmatic series in the ophiolite have

$\varepsilon_{\text{Nd}}(t) \approx +7$ – 8 , similar to modern ridges (Amri et al., 2007; Godard et al., 2006; Haase et al., 2015; McCulloch et al., 1981; Rioux et al., 2012, 2013; Tsuchiya et al., 2013), although whole rock data from boninitic lavas in the upper part of the V2 series have lower values of $\varepsilon_{\text{Nd}}(t) = +0.88$ to $+5.69$ (Kusano et al., 2017). In contrast, published data from the felsic mantle dikes in Oman and the UAE have $\varepsilon_{\text{Nd}}(t) = -7.8$ to $+7.8$, typically with $\varepsilon_{\text{Nd}}(t) < 0$ (Amri et al., 2007; Briquieu et al., 1991; Cox et al., 1999; Haase et al., 2015; Rioux et al., 2013, 2021).

3. Previous Work

Several previous studies have addressed the origin of the felsic mantle dikes. The dikes were first identified and mapped as small biotite granite intrusions into the upper mantle and lowermost crust in the Haylayn and Wuqbah massifs (Browning & Smewing, 1981; Lippard et al., 1986). Geochemical analyses on two dikes from Oman and the UAE showed that the dikes are enriched in LREE and one dike yielded a low $\varepsilon_{\text{Nd}}(t) = -4.1$, suggesting a source with a time-integrated LREE enrichment. Based on the geochemical and isotope data and a K-Ar date from the UAE dike of 85 ± 3 Ma, these authors interpreted the dikes to reflect melting of continental material during obduction of the ophiolite over the Arabian margin. Using the same data, Pearce (1989) similarly concluded that the dikes were related to melting of turbidite deposits on the Arabian continental rise during initial obduction.

To further constrain the origin of the felsic mantle dikes, Briquieu et al. (1991) carried out whole rock geochemical and Pb, Nd, and Sr isotopic analyses of (i) felsic mantle dikes from the UAE and (ii) metamorphic rocks from the Asimah-Masafi metamorphic sole locality and Bani Hamid thrust sheet. They found that the isotopic composition of the dikes was intermediate between a mantle source and more enriched, continental values. Based on these data, they argued that the dikes formed by melting of amphibolite and metasediments in the metamorphic sole of the ophiolite, during initial thrusting of the ophiolite over adjacent crust, with the residual heat of the ophiolite mantle acting as the heat source for sole metamorphism and melting. This model mirrored the conclusions of Boudier et al. (1988), who discussed the link between felsic mantle dikes and mantle shear zones. In a more limited study, Peters and Kamber (1994) presented geochemical data from the felsic dikes in the UAE. Based on comparisons to the quartz diorite to tonalite suite in the ophiolite crust, they argued that the dikes could reflect either extreme fractionation of mantle derived magmas or hydrous partial melting of the ophiolite crust or mantle, with the enriched isotopic compositions attributed to addition of a fluid component derived from the metamorphic sole.

Cox et al. (1999) carried out a detailed major element, trace element, and isotopic study of felsic intrusions throughout the UAE. Their data supported the conclusion of Briquieu et al. (1991) that the dikes reflect mixing between metabasalt and metasedimentary partial melts. They similarly argued that the metasedimentary source had a composition similar to the Bani Hamid granulites and the metabasaltic source was compositionally similar to amphibolites preserved in the metamorphic sole (or equivalent un-metamorphosed volcanic units in the Haybi complex). Using whole-rock elemental and isotopic data, they argued that the dikes formed through both dehydration and fluid saturated melting at pressures of 0.3–0.5 GPa. Cox et al. (1999) attributed formation of the dikes to metamorphism and melting at the top of a subducting slab.

In the Oman portion of the ophiolite, Amri et al. (2007) reported major element, trace element, and Nd and Sr isotopic data for numerous felsic mantle dikes, ultimately attributing their petrogenesis to mixing between a depleted mantle source, a hydrothermal component, and potentially a component of terrigenous sediment. Four recent studies have addressed the origin of the Oman dikes in more detail. Haase et al. (2015) focused on the cluster of intrusions in the southern Haylayn massif, previously studied by Browning and Smewing (1981) and Lippard et al. (1986). They noted mixing trends in major element, trace element, and Hf isotopic data versus MgO, and argued for two-component mixing between sediment melts derived from the top of a subducting slab and basalts formed by partial melting of the overlying mantle wedge. Rollinson (2014a, 2015) presented additional whole rock geochemical data from felsic intrusions from the same area in the Haylayn massif, a cluster of intrusions in the Fizh massif, and intrusions in the UAE portion of the ophiolite. Focusing on dikes with the least fractionated compositions, he suggested that xenocrystic calcic plagioclase, small mafic inclusions within the dikes, and major and trace element variations were consistent with a component of melted amphibolite. Rollinson (2014a, 2015) concluded that the dikes formed by three-component mixing between partial melts derived from amphibolite- to

granulite-facies meta-basalts in a subducted slab, partial melts of subducted sediment from the top of the slab, and assimilation of orthopyroxene and amphibole from harzburgites during ascent of the slab melts through the mantle wedge. In a complementary study, Spencer et al. (2017) carried out oxygen isotope analyses on felsic mantle dikes in Oman and the UAE. The dikes recorded elevated zircon $\delta^{18}\text{O} = 14\text{--}18\text{‰}$, which the authors attributed to melting of pelitic or siliceous sediment on the top of a subducted plate.

In a companion study to this manuscript (Rioux et al., 2021), we present new high-precision U-Pb dating, which constrains the timing of dike intrusion relative to formation of the ophiolite crust, as well as age variations in the felsic mantle dikes along the length of the ophiolite. Our previous work has shown that gabbros related to the V1 volcanic series, the main phase of crustal growth in the ophiolite, yield zircon dates of 96.1–95.6 Ma (Rioux et al., 2012, 2016), indicating rapid crustal growth. Plutonic rocks associated with the V2 magmatic series yield slightly younger dates of 95.6–95.2 Ma (Rioux et al., 2013, 2021). The rapid formation of the crust is consistent with ophiolite formation along an NNW-SSE oriented spreading ridge (present geographical reference frame), parallel to the trend of the sheeted dikes. Our new U-Pb zircon analyses from four felsic mantle dikes from Oman yielded dates from 95.2–95.0 Ma, in agreement with our previous results from two additional samples (95.2–95.1 Ma) (Rioux et al., 2013), indicating intrusion at the end of crustal growth (Rioux et al., 2021). A single dike from the Sarami massif yielded an older date of 95.478 ± 0.032 Ma (discussed below). In contrast to the near synchronous dates throughout Oman, five dated dikes from the UAE yielded significantly younger and highly variable dates from 94.1 to 91.0 Ma (Rioux et al., 2021). The distinct U-Pb dates from the Oman and UAE dikes indicate that the two intrusive series crystallized $\sim 0.9\text{--}4.0$ million years apart. To better constrain the origin of the felsic dikes and assess their chemical heterogeneity along the length of the ophiolite, we here report whole rock major and trace element data for the dated dikes from Oman, two of the dated dikes from the UAE, and a larger geochemical data set from undated intrusions in Oman.

4. Samples

The studied samples come from intrusions into the mantle and lowermost crust along the length of the ophiolite (Figure 1 and Table 1). Five of the samples were collected by Rioux and Garber in Oman. Three are tonalite to trondhjemite intrusions into the mantle section (13211M02, 13215M08, 13221M05) and one is a tonalite intrusion into layered gabbros just above the crust-mantle boundary (13219M03), these intrusions are from the Bahla, Fizh, Wadi Tayin, and Haylayn massifs, respectively. These samples have yielded Th-corrected $^{206}\text{Pb}/^{238}\text{U}$ dates of 95.201 ± 0.032 to 94.95 ± 0.10 Ma, with $\varepsilon_{\text{Nd}}(t) = -1.63$ to -5.05 (Table 2) (Rioux et al., 2021). The fifth sample from Oman, a tonalite that intrudes mantle harzburgite in the Sarami massif (13217M01), yielded a slightly older date of 95.478 ± 0.032 Ma and higher $\varepsilon_{\text{Nd}}(t) = 7.35$ (Rioux et al., 2021). Two additional samples were collected by Searle in the UAE. MS13-1 is a garnet, muscovite, biotite leucogranite from a swarm of felsic intrusions into peridotite in Wadi Hulw bin Sulayman. MS13-5 comes from a series of intrusions at Ra's Dadnah, which include two distinct compositions: a first suite of biotite-hornblende to biotite granite intrusions and a nearby suite of peraluminous leucogranites containing andalusite, cordierite, garnet, biotite, and tourmaline. MS13-5 is a tourmaline-garnet leucogranite from the latter suite. These samples yielded Th-corrected $^{206}\text{Pb}/^{238}\text{U}$ dates of 94.119 ± 0.057 Ma (MS13-1) and 92.361 ± 0.026 Ma (MS13-5), with $\varepsilon_{\text{Nd}}(t) = -4.96$ and -4.63 , respectively.

All remaining dike samples were collected by Amri, Ceuleneer, and Benoit. Sm-Nd and Rb-Sr isotopic data and some whole-rock geochemical data for these samples were previously discussed by Amri et al. (2007); however, the full datasets were not reported in that contribution and are reported here (Table 3). The analyzed samples include granite, tonalite, and quartz diorite intrusions into mantle peridotite and a single tonalite intrusion into lower crustal layered gabbros (94M375). An intrusion adjacent to sample 94M375 previously yielded a U-Pb zircon date of 95.063 ± 0.062 Ma (Rioux et al., 2013).

Finally, to better constrain the composition of underthrust sediment, we also present trace element data from a single garnet- and muscovite-rich metasediment (13222M06; Table 2) collected by Rioux and Garber from ~ 12 m below the Samail Thrust at the Green Pool sole locality in the Wadi Tayin massif. Nd isotope and major element data have previously been reported by Rioux et al. (2016) and Garber et al. (2020), respectively. The metasediment is composed of quartz + white-mica + biotite + plagioclase + garnet + ilmenite + magnet-

Table 1
Sample Locations and Descriptions

Sample	UTM (E) ^a	UTM (N) ^a	IGSN ^b	Location	Rock type
Felsic mantle dikes, Oman—This study and Rioux et al. (2021)					
13211M02	522884	2542834	MER302112	Bahla massif	trondhjemite intruding peridotite
13215M08	424505	2706290	MER302158	Fizh massif	trondhjemite intruding peridotite
13217M01	462,778	2651893	MER302171	Sarami massif	tonalite intruding peridotite
13219M03	520423	2606267	MER302193	Haylayn massif	tonalite intruding layered gabbro
13221M05	623594	2514217	MER302215	Wadi Tayin massif	tonalite intruding peridotite
Felsic mantle dikes, UAE—This study and Rioux et al. (2021)					
MS13-1	422411	2787266	MERMS1301	Khor Fakkan massif	gar.-musc. granite int. peridotite
MS13-5	436536	2822486	MERMS1305	Khor Fakkan massif	gar. granite intruding peridotite
Sole metasediment, Oman—This study, Rioux et al. (2016), Garber et al., (2020)					
13222M06	663854	2550840	MER302226	Wadi Tayin massif	garnet muscovite schist
Felsic mantle dike, Oman—This study and Amri et al. (2007) ^c					
92FZ401A	426899	2712655	MER000002	Fizh massif	granite intruding peridotite
92FZ401C	426899	2712655	MER000003	Fizh massif	granite intruding peridotite
98F15	427643	2722691	MER000004	Fizh massif	tonalite intruding peridotite
98F16	427589	2721971	MER000005	Fizh massif	granite intruding peridotite
97RU7	501529	2620220	MER000006	Haylayn massif	granite intruding peridotite
97RU8	502753	2620829	MER000007	Haylayn massif	granite intruding peridotite
93FR601	427074	2614516	MER000008	Wuqbah massif	tonalite intruding peridotite
94M375	615861	2559433	MER000009	Semail massif	tonalite intruding layered gabbro
98T31A	615001	2524492	MER00000A	Wadi Tayin massif	tonalite intruding peridotite
98T31B	615001	2524492	MER00000B	Wadi Tayin massif	tonalite intruding peridotite
98T31C	615001	2524492	MER00000C	Wadi Tayin massif	quartz diorite intruding peridotite

^aWGS 84, UTM zone 40. ^bAssigned international geo sample number (IGSN). ^cUTM estimated from mapped sample locations.

ite and occurs as a m-scale layer within a section of amphibolite, see Garber et al. (2020) for a detailed discussion of the petrogenesis and field relations.

5. Methods and Results

Geochemical data were analyzed at the Washington State University GeoAnalytical Lab; the Center de Recherches Pétrographiques et Geochimiques (CRPG) at the Université de Lorraine; the Observatoire Midi-Pyrénées (OMP), Unités Mixtes de Recherche (UMR) 556, Toulouse; and Institut Universitaire Européen de la Mer (IUEM), UMR6538, Plouzané. For the Washington State analyses (Table 2), major and minor elements were analyzed on fused beads by x-ray fluorescence, following the procedures of Johnson et al. (1999). Trace element analyses were carried out by inductively coupled plasma-mass spectrometry (ICP-MS) using a combined fusion-acid digestion method, following the procedures of Knaack et al. (1994). Estimates of analytical precision are provided in Table 2, based on comparison of repeat analyses of 250 unknowns for the XRF data (Kelly, 2018) and 50 analyses of the AGV-1 standard over 5 years for the ICP-MS data (Steenberg et al., 2017). The accuracy of Washington State XRF analyses has been estimated as the relative percent difference between regressions of measured versus reported values for certified reference materials, with deviations of 0.03% (Na₂O) to 4.1% (TiO₂), with an average of 1.6% for major elements, and an average deviation of 3.1% for trace elements, with elevated values for Zr (7.7%) and Y (8.5%) (Kelly, 2018). The accuracy of Washington State ICP-MS analyses has been estimated from the relative percent difference from consensus values of 100 analyses of certified reference materials over 5 years; percent differences range from 1.6% to 9.0%, with values ≤3.1% for all elements except Sm, Eu, Tb, Dy, Ho, and Er (4.8%–9.0%)

Table 2
Whole Rock Major Element and Trace Element Data for Samples Analyzed at Washington State

Sample	13211M02	13215M08	13217M01	13219M03	13221M05	MS13-1	MS13-5	13222M06 ^b	Precision ^c
Rock type	trondhjemitic	trondhjemitic	Tonalite	tonalite	tonalite	granite	granite	sole metased.	
Massif	Bahla	Fizh	Sarami	Haylayn	Wadi Tayin	Khor Fakkkan	Khor Fakkkan	Wadi Tayin	±2s%
Zircon date (Ma) ^a	95.201 ± 0.032	95.184 ± 0.065	95.478 ± 0.032	95.126 ± 0.022	94.95 ± 0.10	94.119 ± 0.057	92.361 ± 0.026		
XRF major elements (wt. %)									
SiO ₂	78.07	76.62	71.32	72.81	76.88	75.78	77.90	76.12	0.01–0.02
TiO ₂	0.059	0.018	0.354	0.348	0.201	0.157	0.028	0.488	2–34
Al ₂ O ₃	12.90	13.07	16.11	11.92	13.36	13.24	13.53	10.42	0.4–0.6
FeO*	0.60	0.34	0.80	3.27	1.27	1.12	0.33	4.49	3–20
MnO	0.014	0.012	0.012	0.115	0.016	0.099	0.013	0.161	1–8
MgO	0.23	0.10	0.89	2.89	0.60	0.52	0.20	2.18	1–31
CaO	1.59	0.74	2.93	4.23	1.63	1.40	1.76	0.99	1–3
Na ₂ O	4.63	3.14	5.03	2.14	4.64	2.95	5.69	1.57	0.5–2.5
K ₂ O	1.67	5.50	1.08	0.38	0.91	4.71	0.12	2.17	0.2–17.8
P ₂ O ₅	0.022	0.023	0.094	0.149	0.028	0.072	0.023	0.046	3–24
Sum	99.79	99.56	98.62	98.25	99.53	100.05	99.60	98.63	
XRF trace elements (ppm)									
Ni	2	4	26	77	2	8	2	46	5–85
Cr	4	3	2	47	5	8	3	60	5–79
Sc	4	3	29	12	10	3	2	12	4–40
V	1	1	6	96	8	22	5	83	4–140
Ba	265	592	96	33	52	206	8	176	1–88
Rb	36	110	11	11	10	140	1	85	1–77
Sr	76	67	236	179	176	97	120	100	1–4
Zr	53	43	11	98	67	92	56	94	3–17
Y	29	17	29	23	39	29	52	22	2–6
Nb	7.4	14.7	1.3	9.5	4.4	16.2	6.5	8.7	5–54
Ga	11	10	15	11	14	13	12	13	9–14
Cu	1	1	0	5	8	2	1	32	7–393
Zn	4	5	5	35	21	30	3	80	4–11
Pb	23	66	2	6	13	26	20	10	3–48
La	13	9	3	22	9	22	17	23	15–82
Ce	24	21	0	50	14	47	32	50	9–30
Nd	8	9	4	20	6	18	16	8	13–59
Th	5	6	0	6	2	10	15	20	4–46
U	2	7	0	2	1	1	2	2	
ICP-MS trace elements (ppm)									
La	13.23	13.01	0.90	22.16	8.33	22.32	15.29	23.14	1.2
Ce	25.04	26.66	2.39	47.80	15.24	49.82	36.90	49.95	1.1

Table 2
Continued

Sample	13211M02	13215M08	13217M01	13219M03	13221M05	MS13-1	MS13-5	13222M06 ^b	Precision ^c
Pr	2.57	2.88	0.47	5.27	1.61	5.22	4.19	5.35	1.5
Nd	8.84	10.19	3.08	20.02	6.03	19.08	16.51	19.61	1.9
Sm	1.96	2.37	1.74	4.36	1.69	4.55	4.90	3.91	2.9
Eu	0.35	0.59	0.79	1.11	0.46	0.92	0.52	0.84	2.6
Gd	2.41	2.40	3.28	4.23	2.80	4.47	5.90	3.50	2.2
Tb	0.50	0.43	0.69	0.69	0.63	0.78	1.11	0.57	3.5
Dy	3.74	2.71	4.81	4.09	4.97	4.58	7.41	3.56	2.3
Ho	0.94	0.58	1.08	0.80	1.29	0.94	1.61	0.74	2.1
Er	2.95	1.66	3.03	2.10	4.10	2.59	4.42	2.07	2.5
Tm	0.47	0.25	0.43	0.30	0.67	0.39	0.65	0.31	3.4
Yb	3.17	1.65	2.59	1.78	4.66	2.50	4.07	1.98	2.2
Lu	0.56	0.26	0.41	0.28	0.83	0.39	0.62	0.32	3.9
Sc	3.85	1.99	28.78	11.91	9.88	4.32	1.99	11.66	3.4
Rb	36.15	112.11	11.49	10.70	10.32	139.31	1.65	84.85	1.7
Sr	80.08	71.48	240.02	182.93	177.24	99.77	125.51	103.71	1.3
Y	27.26	16.39	26.41	20.90	35.00	26.53	46.71	19.34	1.5
Zr	52.64	42.87	10.57	99.29	68.34	92.06	57.28	95.03	2.2
Nb	6.65	13.33	0.85	8.71	3.84	15.33	6.16	8.09	1.7
Cs	0.55	6.97	0.15	0.24	0.23	4.89	0.04	3.30	3.7
Ba	270.11	604.33	97.55	31.14	52.43	210.49	8.98	178.71	2.2
Hf	1.52	1.62	0.58	2.36	1.99	2.77	2.43	2.62	2.0
Ta	0.48	2.52	0.04	0.61	0.25	1.12	0.65	0.65	2.9
Pb	21.86	62.62	0.60	5.36	11.13	23.52	18.47	9.62	1.7
Th	5.23	5.81	0.07	5.84	2.35	9.42	14.89	8.76	2.2
U	2.38	6.22	0.10	1.32	0.96	1.51	2.44	1.28	2.2
ID-TIMS Sm-Nd isotopic data ^d									
Sm	2.26	2.43	1.70	4.38	1.72	4.75	5.38	3.88	
Nd	10.62	10.45	3.12	19.87	6.68	19.83	18.13	20.30	
¹⁴⁷ Sm/ ¹⁴⁴ Nd	0.1284	0.1405	0.3290	0.1331	0.1559	0.1447	0.1794	0.1155	
±2σ	0.0012	0.0012	0.0028	0.0012	0.0014	0.0012	0.0016	0.0010	
¹⁴³ Nd/ ¹⁴⁴ Nd	0.512346	0.512451	0.513098	0.512339	0.512529	0.512351	0.512390	0.512159	
±2σ	0.000008	0.000008	0.000042	0.000010	0.000008	0.000010	0.000006	0.000003	
ε _{Nd} ⁽⁹⁶⁾	-4.86	-2.96	7.35	-5.05	-1.63	-4.96	-4.63	-8.35	

^aTh-corrected weighted mean or single grain ²⁰⁶Pb/²³⁸U crystallization ages from Rioux et al. (2021). ^bMajor element data previously reported by Garber et al. (2020). ^cReported precision of the XRF data calculated as the 2σ enclosure values following Kelly (2018); precision scales with concentration, within the reported range. ICP-MS precision estimated from 50 repeat analyses of AGV-1 over five years. ^dSm-Nd isotopic data from Rioux et al. (2021) and Rioux et al. (2016), analyzed at MIT. Reported ¹⁴³Nd/¹⁴⁴Nd are current values.

(Steenberg et al., 2017). For the OMP-CRPG-IUEM data (Table 3), whole rock major and minor elements were analyzed on fused glass beads by XRF at CRPG. Trace element analyses were again carried out by ICP-MS using a combined lithium borate fusion-acid digestion procedure at UMR5563-OMP; analytical procedures and accuracy are discussed in Aries et al. (2000) and Braun et al. (1998). Nd and Sr isotopes were measured following the procedure described in Amri et al. (2007) at UMR6538, IUEM, Plouzané.

The major and trace element data are summarized in Figures 2–7, Tables 2 and 3, and Supplemental Figure S1. The analyzed dikes have 71.3–78.1 wt. % SiO₂, with the exception of a single quartz diorite with 57.4 wt. % SiO₂ (98T31C, Wadi Tayin massif, Table 3). Compared to the V1 and V2 plutonic rocks from the ophiolite crust, dikes from the Wadi Tayin, Bahla, northern Haylayn, Sarami, and Fizh massifs in the Oman portion of the ophiolite have high K₂O (up to 5.5 wt. %; Figures 2e and 3f), and are generally peraluminous (Figure 2c; Other Oman symbols), implying elevated Al₂O₃ relative to feldspar stoichiometry; the single low SiO₂ quartz diorite intrusion is metaluminous. Chondrite-normalized REE patterns from the intrusions at these localities range from U- and V-shaped to LREE enriched with flat heavy REE (HREE), with the exception of 13217M01, which has an LREE depleted pattern (Figure 4c). The intrusions are depleted in Ti and enriched in Rb, Ba, K, Pb, Th, and U, and to a lesser extent Ta and Nb, relative to the V1 and V2 volcanic rocks from the ophiolite (Figure 4).

In contrast to the other Oman dike localities, published data (Haase et al., 2015; Rollinson, 2014a, 2015) and a single datum from this study from the Wadi Hajr and Wadi Hemli intrusions in the southern Haylayn massif include both metaluminous and peraluminous compositions, have higher MgO, and have lower K₂O on average (“Haylayn” symbols in Figures 2 and 3). These intrusions generally have LREE-enriched and relatively flat HREE chondrite-normalized patterns (Figure 4b); in all of the Oman dike samples, only a few rare samples show significant HREE depletion. Much of the previous research on the Oman dikes have focused on the Wadi Hajr and Wadi Hemli intrusions (Haase et al., 2015; Rollinson, 2014a, 2015), although Rollinson (2015) also studied dikes from a locality in the Fizh massif.

In the UAE, published data (Cox et al., 1999; Rollinson, 2015) and the two samples from this study overlap the non-Haylayn Oman dikes. The UAE data primarily plot within the peraluminous field, with a smaller number of metaluminous and peralkaline samples (Figure 2d), and are elevated in K₂O, relative to the V1 and V2 plutonic rocks (Figures 2f and 3f). Data from Ra’s Dibba and Ra’s Dadnah extend to more peraluminous compositions than the Oman data, which is consistent with the observed presence of Al-rich minerals in these intrusions, including garnet, cordierite, and andalusite (Cox et al., 1999). Excluding Al Bithnah, REE patterns range from LREE enriched with flat HREE to nearly flat REE patterns with extreme negative Eu anomalies (Figure 4d; discussed in detail by Rollinson, 2015). In contrast, samples from Al Bithnah have steep LREE enriched and HREE depleted patterns, small positive or no Eu anomalies, and higher K₂O (Figures 2f and 4d).

The sediment (13222M06) from the Wadi Tayin metamorphic sole locality is characterized by LREE enrichment with flat HREE; Rb, Ba, Th, U, K, Ta, and Nb enrichment relative to MORB and the V1 lavas in the ophiolite; and Nb and Ta depletion relative to other incompatible trace elements (Figure 4a).

The Nd and Sr isotopic data for the felsic mantle dike samples in this study have previously been discussed by Rioux et al. (2021) and Amri et al. (2007) (Tables 2 and 3). Whole rock isotopic values from the samples range from $\epsilon_{\text{Nd}}(t) = -5.8$ to $+4.1$, with two higher datum of $\epsilon_{\text{Nd}}(t) = +7.4$ and $+7.8$ (Figure 5) and $^{87}\text{Sr}/^{86}\text{Sr}_{\text{int.}} = 0.703763$ to 0.709404 . The Nd and Sr data are correlated, with high ϵ_{Nd} corresponding to lower $^{87}\text{Sr}/^{86}\text{Sr}$. The sole metasediment has an $\epsilon_{\text{Nd}}(t) = -8.35$ (Rioux et al., 2016).

6. Discussion

6.1. Origin of the Felsic Mantle Dikes in the Oman Portion of the Ophiolite

Given the significant age differences between the felsic mantle dikes in the southern (Oman) and northernmost (UAE) portions of the ophiolite, we discuss their origin separately. We start with the Oman dikes, which intruded at the end of crystallization of the oceanic crust of the ophiolite. Figures 5 and 6 illustrate the geochemical trends discussed below, with plot symbols grouped and colored based on the distribution of dike compositions on plots of MgO or SiO₂ versus $\epsilon_{\text{Nd}}(t)$ (Figures 5a and 5b). On these plots, the data from

Table 3
Whole Rock Major Element, Trace Element, and Isotope Data for Samples Analyzed at University de Lorraine and Observatoire Midi-Pyrénées

Sample	92FZ401A	92FZ401C	98F15	98F16	97RU7	97RU8	93FR601	94M375	98T31A	98T31B
Rock type	Granite	Granite	Tonalite	Granite	Granite	Granite	Tonalite	Tonalite	Tonalite	Tonalite
Massif	Fizh	Fizh	Fizh	Fizh	Haylayn	Haylayn	Wuqbah	Semail	Wadi Tayin	Wadi Tayin
XRF major elements (wt. %)										
SiO ₂	76.75	77.12	77.91	77.59	77.58	74.70	73.95	74.80	76.32	71.78
TiO ₂			0.100	0.080		0.100	0.110	0.200	0.170	0.210
Al ₂ O ₃	12.87	12.64	12.48	12.36	12.85	13.02	12.43	13.30	13.18	13.41
FeO*	1.05	1.08	0.87	0.69	0.31	1.03	0.77	1.58	1.25	4.21
MnO	0.000	0.000	0.000	0.000	0.000	0.030	0.000		0.000	0.080
MgO	0.40	0.52	0.26	0.33	0.23	0.44	2.86	0.53	0.66	0.93
CaO	2.10	1.03	1.05	1.13	1.32	1.66	0.72	2.27	2.68	4.05
Na ₂ O	3.78	3.11	4.80	3.46	3.30	2.99	5.85	4.54	3.59	2.47
K ₂ O	2.02	4.51	1.81	3.76	3.79	4.18	0.16	1.10	0.96	1.03
P ₂ O ₅	0.000	0.050	0.000	0.000	0.000	0.050	0.060		0.060	0.000
LOI	0.420	0.190	0.360	0.260	0.290	1.300	2.150		0.750	1.100
Sum	99.51	100.37	99.74	99.74	99.70	99.78	99.15		99.76	99.74
ICP-MS trace elements (ppm)										
La	24.36	17.94	9.21	4.31	16.48	22.44	6.41	2.27	6.10	4.17
Ce	46.73	35.93	19.46	7.47	37.64	51.78	13.09	4.99	11.63	8.14
Pr	4.63	3.59	2.24	0.71	3.67	4.98	1.40	0.64	1.24	0.88
Nd	16.71	12.93	9.54	2.64	12.59	18.37	5.80	2.93	4.64	3.56
Sm	2.71	2.67	2.23	0.57	2.56	3.76	1.45	0.87	1.16	1.06
Eu	0.91	0.61	0.28	0.11	0.59	0.80	0.27	0.44	0.36	0.29
Gd	1.81	2.61	2.17	0.56	2.00	3.34	1.86	1.04	1.80	1.79
Tb	0.21	0.48	0.37	0.09	0.33	0.56	0.35	0.18	0.38	0.39
Dy	1.13	3.10	2.53	0.67	1.90	3.46	2.58	1.05	3.14	3.11
Ho	0.22	0.64	0.59	0.15	0.38	0.70	0.62	0.22	0.74	0.75
Er	0.67	2.06	2.00	0.57	1.09	2.03	2.21	0.67	2.67	2.64
Tm	0.10	0.31	0.33	0.10	0.16	0.29	0.36	0.09	0.44	0.42
Yb	0.81	2.16	2.56	0.79	1.13	1.96	2.86	0.66	3.32	3.17
Lu	0.15	0.33	0.46	0.16	0.17	0.28	0.50	0.10	0.56	0.52
Sc	67.81	62.97	56.22	60.53	61.25	59.41	65.45	12.81	48.27	63.38
Rb	57.05	89.77	50.46	83.54	121.79	156.22	8.34	6.81	21.26	20.91
Sr	137.94	76.21	32.17	18.26	92.49	116.83	69.73	137.00	70.76	125.98
Y	6.16	20.77	17.05	4.81	12.22	21.27	20.03	5.44	21.49	20.92
Zr	92.83	51.49	65.62	53.60	35.09	81.64	77.55	3.17	48.54	23.80
Nb	4.54	9.30	2.51	1.26	9.47	10.68	2.65	0.70	1.85	1.76
Cs	3.13	3.89	2.51	2.46	7.35	11.90	1.32	0.03	0.81	0.73
Ba	303.21	722.26	185.66	314.60	217.79	272.64	71.79	229.40	148.78	167.60
Hf	2.28	1.65	2.31	1.68	1.21	2.07	2.46	0.26	1.37	0.84
Ta	0.78	1.68	0.25		1.38	1.34	0.26			
Pb	28.17	43.42	12.27	21.36	32.64	33.04	8.74	2.97	15.66	13.64
Th	7.13	6.27	3.57	2.01	6.48	8.42	2.53	0.38	1.88	1.14
U	1.30	2.76	0.64	0.44	2.08	1.99	0.60	0.08	1.11	0.66

Table 3
Continued

Sample	92FZ401A	92FZ401C	98F15	98F16	97RU7	97RU8	93FR601	94M375	98T31A	98T31B
Ti	673.93	469.98	708.34	578.61	391.44	798.47	769.04		1029.06	1284.58
V	1.91	1.95	1.11	3.77		34.14	2.60	6.07	6.30	7.21
Cr	6.44			2.89		3.16	5.50	10.20		
Co	1.65	0.95	0.75	1.39	0.74	1.85	1.01	1.81	1.72	4.82
Ni	7.92	4.08	5.21	8.95	4.24	6.66	5.32	1.29	12.55	18.16
Cu	1.17	0.95	1.98	1.42	0.73	7.92	1.77	6.48	4.60	7.14
Zn	14.51	13.39	14.83	8.94		16.70	6.94	24.64	19.67	75.07
Ga	11.39	11.90	11.47	9.00	10.31	11.66	12.32	14.27	13.33	15.10
Ge	0.78	1.09	1.01	0.85	1.18	1.40	0.76		0.81	1.00
Sn	0.73	0.21	0.42			1.44	0.06	0.22		
Sb	0.21	0.15	0.05	0.19	0.26	0.28	0.12	0.01	0.89	0.29
ID-TIMS Sm-Nd and Rb-Sr isotopic data ^a										
Sm	2.71	2.67	2.23	0.57	2.56	3.76	1.45	0.87	1.16	1.06
Nd	16.70	12.90	9.50	2.60	12.60	18.40	5.80	2.93	4.60	3.60
¹⁴⁷ Sm/ ¹⁴⁴ Nd	0.0981	0.1252	0.1420	0.1326	0.1229	0.1236	0.1512	0.1787	0.1525	0.1781
¹⁴³ Nd/ ¹⁴⁴ Nd	0.512403	0.512442	0.512746	0.512808	0.512303	0.512296	0.512751	0.513027	0.512471	0.512535
±2σ	0.000003	0.000004	0.000003	0.000003	0.000003	0.000005	0.000003	0.000014	0.000003	0.000003
ε _{Nd} ⁽⁹⁶⁾	−3.38	−2.95	2.78	4.10	−5.63	−5.78	2.76	7.81	−2.72	−1.78
Rb	57.05	89.77	50.46	83.54	121.79	156.22	8.34	6.81	21.26	20.91
Sr	138.00	76.00	32.00	18.00	92.00	117.00	70.00	137.00	71.00	126.00
⁸⁷ Rb/ ⁸⁶ Sr	1.162	3.320	4.432	13.060	3.722	3.754	0.335	0.140	0.841	0.466
⁸⁷ Sr/ ⁸⁶ Sr	0.709274	0.712145	0.710373	0.722690	0.713774	0.714525	0.705004	0.703954	0.707873	0.707480
±2σ	0.000008	0.000011	0.000004	0.000006	0.000007	0.000004	0.000010	0.000009	0.000006	0.000003
⁸⁷ Sr/ ⁸⁶ Sr _{int.}	0.707689	0.707616	0.704327	0.704875	0.708697	0.709404	0.704547	0.703763	0.706725	0.706844

^aSm-Nd and Rb-Sr isotopic data from Amri et al. (2007). Reported ¹⁴³Nd/¹⁴⁴Nd are current values.

the Oman felsic mantle dikes define two orthogonal trends. Data from the southern Haylayn massif define a near-horizontal trend of variable MgO with nearly constant ε_{Nd}(t) = −4 to −6 (red symbols). REE patterns from these samples are generally LREE enriched with flat HREE (Figure 6f), similar to metasedimentary sample 13222M06 from the metamorphic sole of the ophiolite (solid black line, Figure 6f). These major and trace element trends and the REE patterns can be explained by mixing or reaction between a low MgO, low ε_{Nd} sediment (±amphibolite) partial melt and a high MgO-Ni mantle component, consistent with the Haase et al. (2015) and Rollinson (2014a, 2015) studies, which focused on this area. Haase et al. (2015) argued that the mantle component is mantle derived basaltic melt, consistent with the increase in TiO₂ concentration with increasing mantle component (Figure 5d), while Rollinson (2014a, 2015) suggests that interaction with mantle harzburgite is a more efficient way to increase the MgO and compatible trace element (e.g., Ni, Cr) concentrations.

Data from felsic mantle dikes from most other areas in Oman define a perpendicular trend to the Haylayn mixing array (green symbols), with variable ε_{Nd}(t) at low MgO (<1 wt %), low Ni (<18 ppm), and high SiO₂ (>70 wt. %) (Figures 5a–5c). At ε_{Nd}(t) > −2, the REE patterns from the dikes are predominantly U- and V-shaped (Figures 6b–6d); dikes with ε_{Nd}(t) < −2 have primarily LREE enriched patterns, with a few V-shaped patterns (Figures 6e and 6f). The U-shaped patterns match the expected REE pattern for partial melts derived from MORB metamorphosed at amphibolite-facies conditions (black dashed line, Figures 6b–6d), due to preferential partitioning of the MREE into amphibole (±clinopyroxene). We hypothesize that the more pronounced V-shaped patterns in some samples (Figure 6d) may result from variations in amphibole

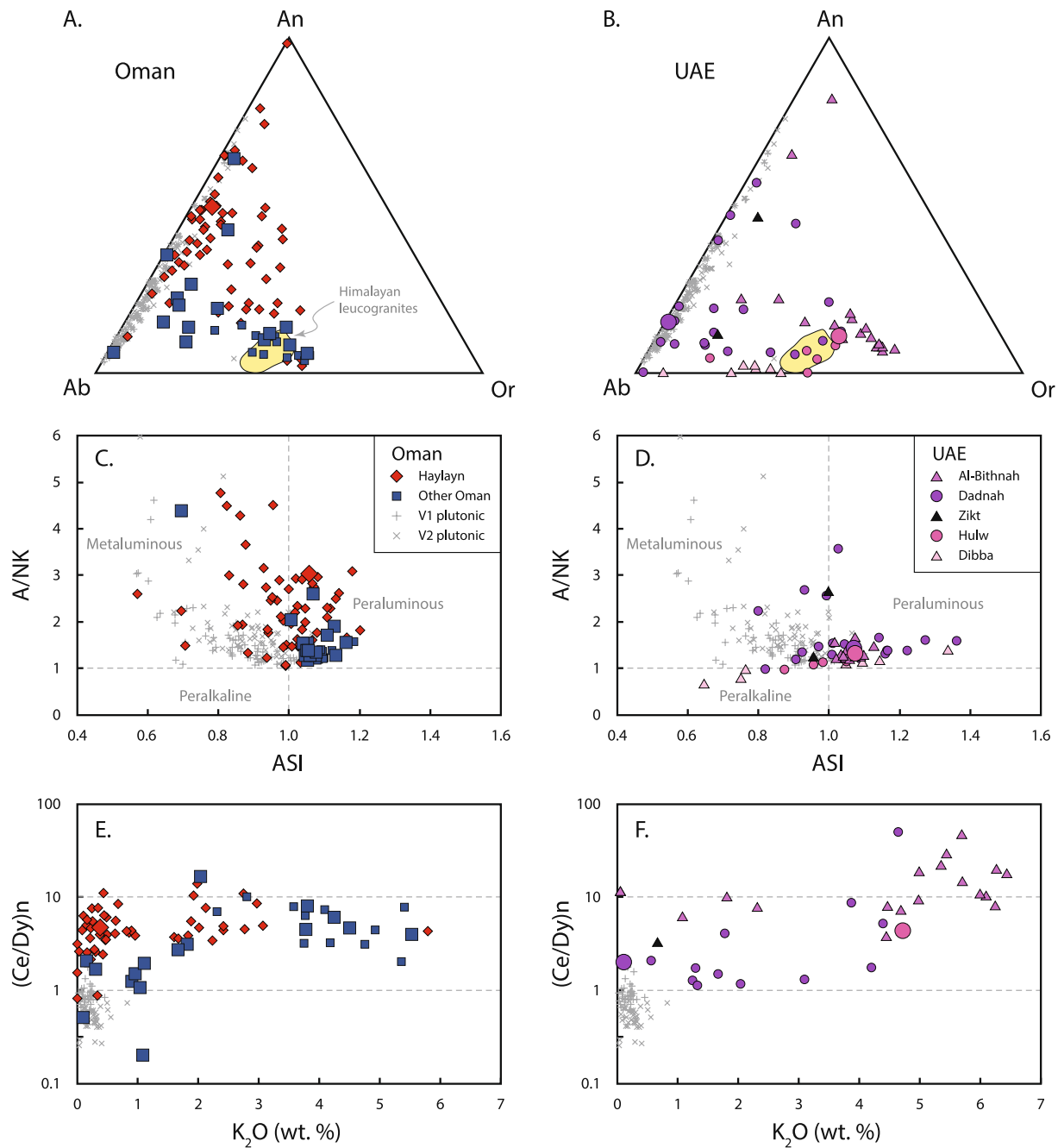


Figure 2. Composition of felsic mantle dikes from Oman ((a), (c), (e)) and the United Arab Emirates (UAE) ((b), (d), (f)). Larger plot symbols denote data from this study. Plutonic rocks associated with the V1 and V2 magmatic series are included for comparison (Haase et al., 2016; Rollinson, 2009). The Haylayn group only includes samples from Wadi Hajr and Wadi Hemli, in the southern Haylayn massif; two samples from the northern Haylayn massif are grouped with the “Other Oman” samples. (a)–(b) CIPW normative compositions of the felsic mantle dikes. Himalayan leucogranites field is after Rollinson (2015), based on data from Guo and Wilson (2012); plutonic fields are after Barker (1979). (c)–(d) Aluminum saturation index (molar $\text{Al}_2\text{O}_3/[(\text{CaO}-3.34*\text{P}_2\text{O}_5)+\text{Na}_2\text{O}+\text{K}_2\text{O}]$) (Frost et al., 2001) versus molar $\text{Al}_2\text{O}_3/(\text{Na}_2\text{O} + \text{K}_2\text{O})$. (e)–(f) Weight percent K_2O versus normalized Ce/Dy. Data sources are listed in Figure 3 caption.

partition coefficients or the impact of additional residual phases during melting, such as titanite (Supplemental Text S1). In this context, we suggest that the low MgO trend (green symbols) is a result of partial melting of underthrust sediment and metabasalt; the low $\epsilon_{\text{Nd}}(t)$ end member (blue symbols) has the highest proportion of sediment-derived partial melts, while the higher ϵ_{Nd} samples (green symbols) are increasingly dominated by partial melts derived from amphibolite- to granulite-facies metabasalts. The correlation

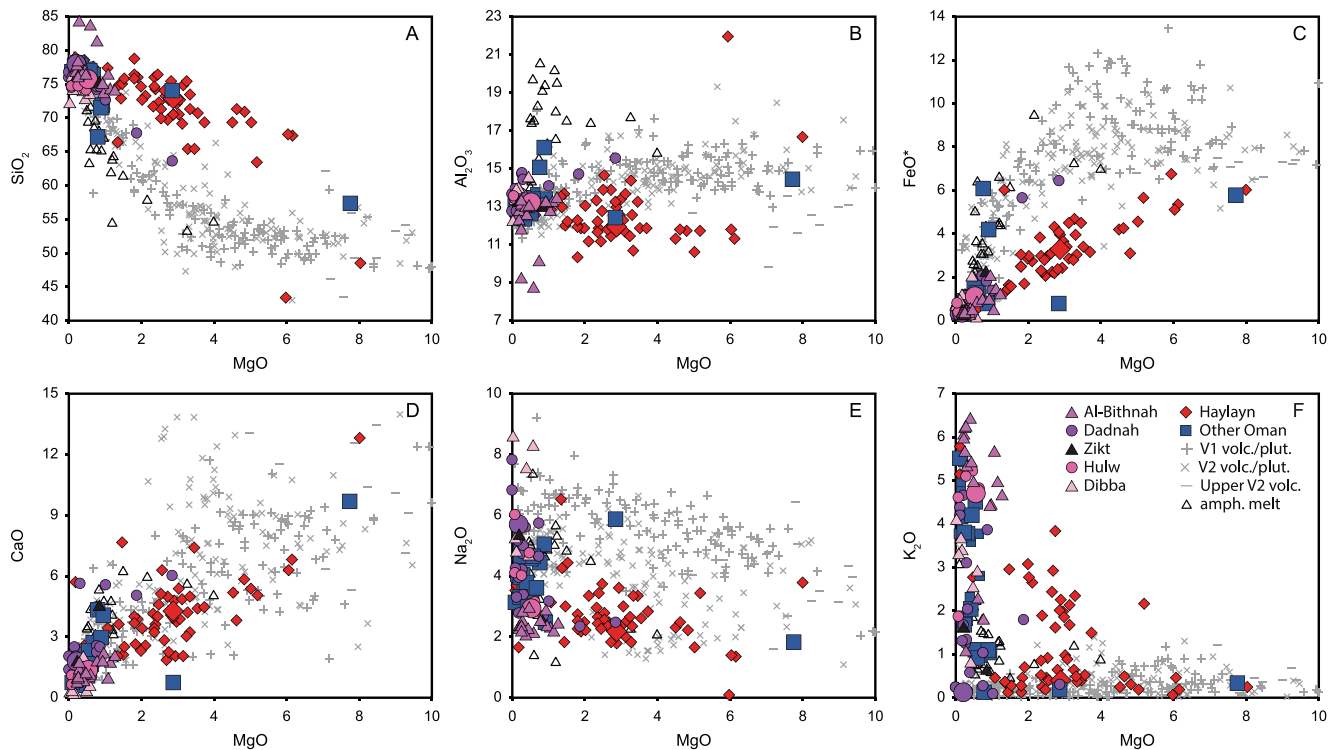


Figure 3. Major element variation diagrams. V1 and V2 data with MgO = 10–14 wt. % plot off scale. Data sources: felsic mantle dikes (this study; Amri et al., 2007; Cox et al., 1999; Haase et al., 2015; Rollinson, 2014a, 2015), V1 and V2 volcanic rocks (Godard et al., 2003, 2006; Kusano et al., 2012, 2014, 2017), V1 and V2 plutonic rocks (Amri et al., 2007; Haase et al., 2016; Rioux et al., 2016; Tsuchiya et al., 2013). The V1 and V2 plutonic rocks are plotted based on how the data were grouped in the source publications; however, we note that robust distinction between the V1 and V2 related plutonic rocks requires a combination of field observations and geochemical data, which are not reported in all studies. The upper V2 volcanic series corresponds to the upper V2 lavas of Kusano et al. (2017), with the addition of a single lower V2 lava with low ϵ_{Nd} (sample 10SH21). “Amph. melt” data are liquid compositions from amphibolite melting experiments by Rapp et al. (1991), Rushmer (1991), and Zhang et al. (2013).

between ϵ_{Nd} and REE patterns cannot be explained by fractional crystallization of amphibole (or any phase) from the felsic dikes, as crystallization does not change isotopic ratios.

The distinct mantle mixing (red symbols) and amphibolite melting (green symbols) trends are apparent in other major and trace element data (Figures 3 and 5). For example, the two datasets display distinct slopes on major element variation diagrams (e.g., Figure 5d). The high SiO_2 , low MgO, and other major element trends are consistent with the observed composition of amphibolite melts from experimental studies at pressures and temperatures similar to those observed in the metamorphic sole of the ophiolite (Figures 3 and 5d) (Rapp et al., 1991; Rushmer, 1991; Zhang et al., 2013).

Patifio Douce (1999) developed major element discrimination diagrams for melts derived from meta-sediments versus meta-basalts, based on a compilation of experimental data. For the Oman mantle dikes, the low MgO, low ϵ_{Nd} sediment-rich end member compositions (blue symbols) plot parallel to the trend of melts derived from felsic metapelites, while the dikes with higher ϵ_{Nd} , and a larger amphibolite component (green symbols), are generally transitional between the compositions of meta-sediment and amphibolite melts (Figure 5e). The Haylayn dikes plot within the amphibolite melt field on this diagram, but this likely reflects mixing with a mantle component; the compositions of mantle-derived magmas overlap the amphibolite melt field, as seen in the V1 and V2 data.

Outside of the amphibolite melting and mantle mixing trends, there are almost no dikes with elevated ϵ_{Nd} (−2 to 4) and high MgO (>2 wt. %), high Ni (>20 ppm), or low SiO_2 (<70 wt. %) (i.e., the center of Figures 5a–5c). The dearth of such data supports our conclusion that the U- and V-shaped REE patterns observed in the amphibolite melting trend reflect REE partitioning during partial melting of amphibolite, rather than amphibole fractionation from compositions along a more positive ϵ_{Nd} (−2 to 4) extension of the

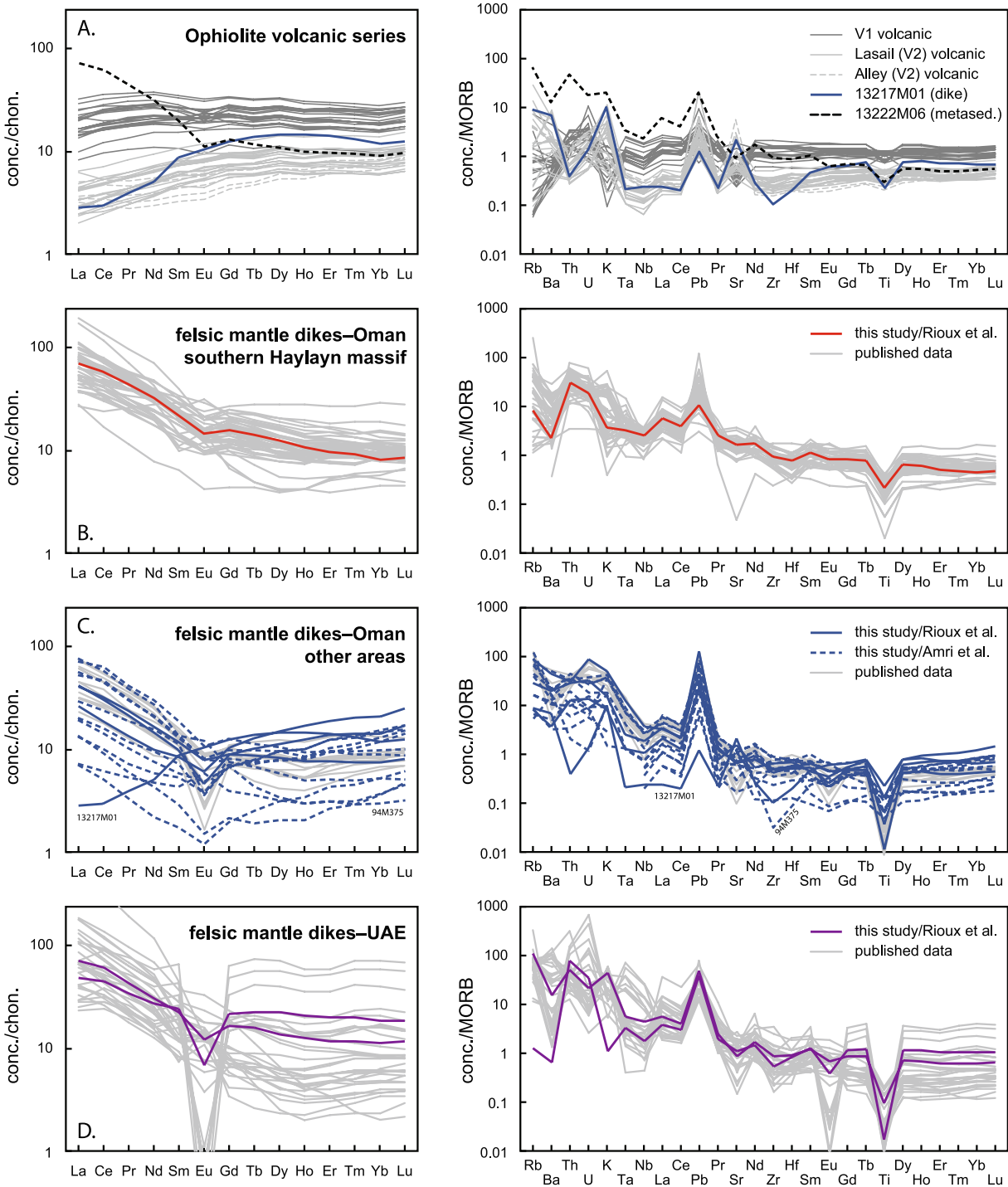


Figure 4. Rare earth element (REE) and extended trace element diagrams for magmatic series in the Samail ophiolite. Panel (a) includes data for the sole metasediment reported herein. Data sources: felsic mantle dikes from the southern Haylayn massif (Wadi Hajr and Wadi Hemli) (Haase et al., 2015; Rollinson, 2014a, 2015); felsic mantle dikes from other areas of Oman (Amri et al., 2007; Rollinson, 2015); felsic mantle dikes in the UAE (Rollinson, 2015); V1 and V2 volcanic rocks (Godard et al., 2003; Godard et al., 2006). For a discussion of the origin of the flat REE patterns with large negative Eu anomalies from the Ra's Dadnah area in the UAE, see Rollinson (2015). REE diagrams are normalized to Anders and Grevesse (1989) multiplied by 1.36 (Korotev, 1996) and extended trace element diagrams are normalized to normal mid-ocean ridge basalt (Hofmann, 1988). Sample 13217M01 is highlighted in panel (a), but is also plotted in panel (c). REE, Rare earth element.

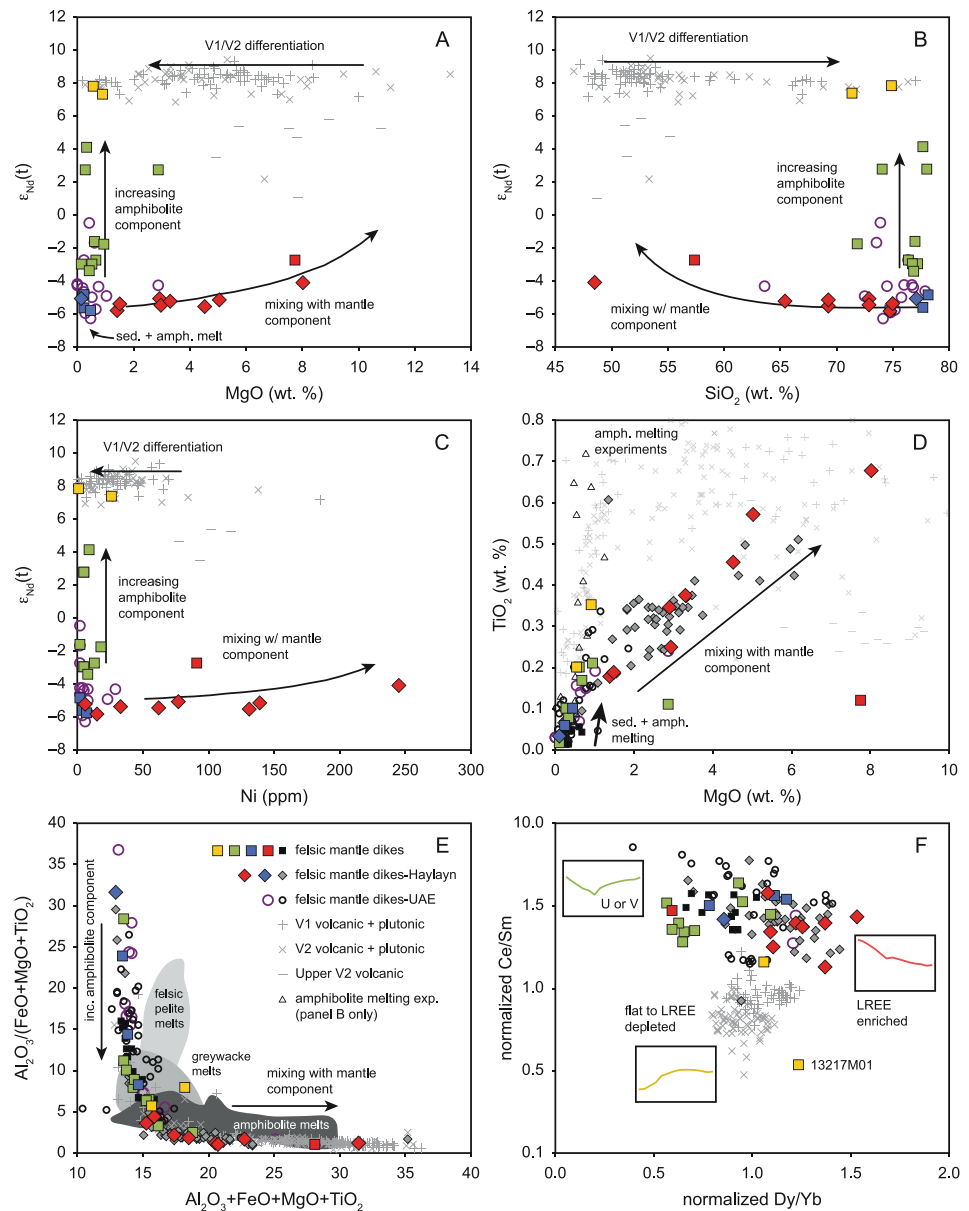


Figure 5. Major element, trace element and isotope variation diagrams. Felsic mantle dikes are divided into intrusions in the southern Haylayn massif (diamonds), intrusions from the rest of the ophiolite sections in Oman (squares), and intrusions in the United Arab Emirates (UAE) portion of the ophiolite (open circles). Symbol colors for the Oman dikes are based on data groupings shown in (a) and described in the text. Smaller gray and black symbols for the dikes in ((d), (e), (f), (g)) correspond to geochemical data that lack Nd isotopic data. The V1 and V2 datasets include analyses from volcanic and plutonic rocks attributed to these magmatic events. Data sources are provided in Supplemental Figure S1. Additional sources include the following: (b) amphibolite melting experiments (Rapp et al., 1991; Rushmer, 1991; Zhang et al., 2013); (e) discrimination diagram (Patiño Douce, 1999; Rollinson, 2015); (h) sediment and amphibolite Zr/Sm (Foley et al., 2002; Guo & Wilson, 2012). Abbreviations: sed., sediment; amph., amphibolite; inc., increasing; exp. experiments.

Haylayn mantle-sediment mixing trend (red diamonds). Differentiation of compositions from the Haylayn trend would likely generate dikes along a constant ϵ_{Nd} chord (-2 to 4) with intermediate MgO, SiO₂, and Ni concentrations, due to crystallization of mafic phases from the MgO-rich compositions, but such compositions are not observed. It is possible that the data reflect a sampling bias, since we largely focused on felsic, MgO poor rocks, and the separation of the two mixing trends could be further tested by additional sam-

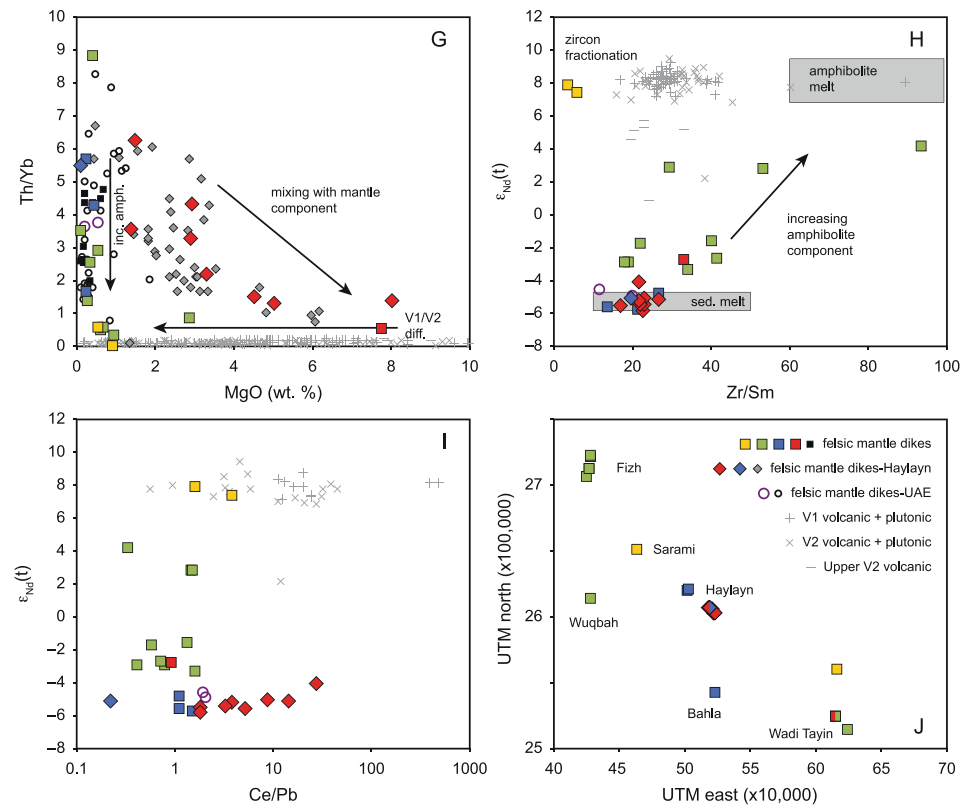


Figure 5. Continued

pling. The two distinct trends also suggest that the Haylayn swarm is unique in incorporating a significant mantle component. The one exception to this is a single sample from the Wadi Tayin massif (98T31C; Amri et al., 2007), which plots within the Haylayn mixing trend (square, red symbol, Figure 5a); two other samples from the same locality plot within the amphibolite melting trend, suggesting significant heterogeneities within dike swarms over small length scales (10–100s of meters). Beyond the concentration of high MgO, low ϵ_{Nd} dikes in the southern Haylayn massif, there are no obvious geographic trends in the isotopic data (Figure 5j).

The low ϵ_{Nd} , low MgO dikes (blue symbols) plot at the confluence of the amphibolite melting and mantle mixing trends and therefore are expected to represent the most sediment-melt rich end members. In our prior work, we showed that metasediment from the Wadi Tayin massif, which we report whole rock geochemical data for here, has $\epsilon_{Nd}(t) = -8.4$ (Rioux et al., 2016, p. 13222M06), suggesting that some sediments thrust below the ophiolite had even lower ϵ_{Nd} than observed in the mantle dikes. Based on this datum, it is possible that even the dikes with the lowest MgO and $\epsilon_{Nd}(t)$ (blue symbols) are a mix of amphibolite with higher $\epsilon_{Nd}(t)$ and sediment melt, rather than pure sediment melts. This conclusion is consistent with Rollinson (2015), who argued that small mafic inclusions and potentially xenocrystic high anorthite cores in the Haylayn dikes are related to amphibolite melting, and successfully modeled the REE patterns and other trace element abundances of the southern Haylayn intrusions (red symbols) as a mix of amphibolite and sediment partial melts (black dashed line, Figure 6f), combined with a mantle component. In contrast, Spencer et al. (2017) argued that zircon and whole-rock oxygen isotope data from the southern Haylayn dikes are best explained by pure sediment melting, with no mantle derived (or amphibolite) component. Our data do not preclude this possibility for some of the lowest MgO and $\epsilon_{Nd}(t)$ samples (blue symbols); however, it is clear from the Ni and MgO data that many of the higher MgO Haylayn dikes contain a mantle component, and similarly, we consider it likely that some or all of the lowest MgO and $\epsilon_{Nd}(t)$ samples (blue symbols) represent a mix of amphibolite and sediment melts, rather than pure sediment melts.

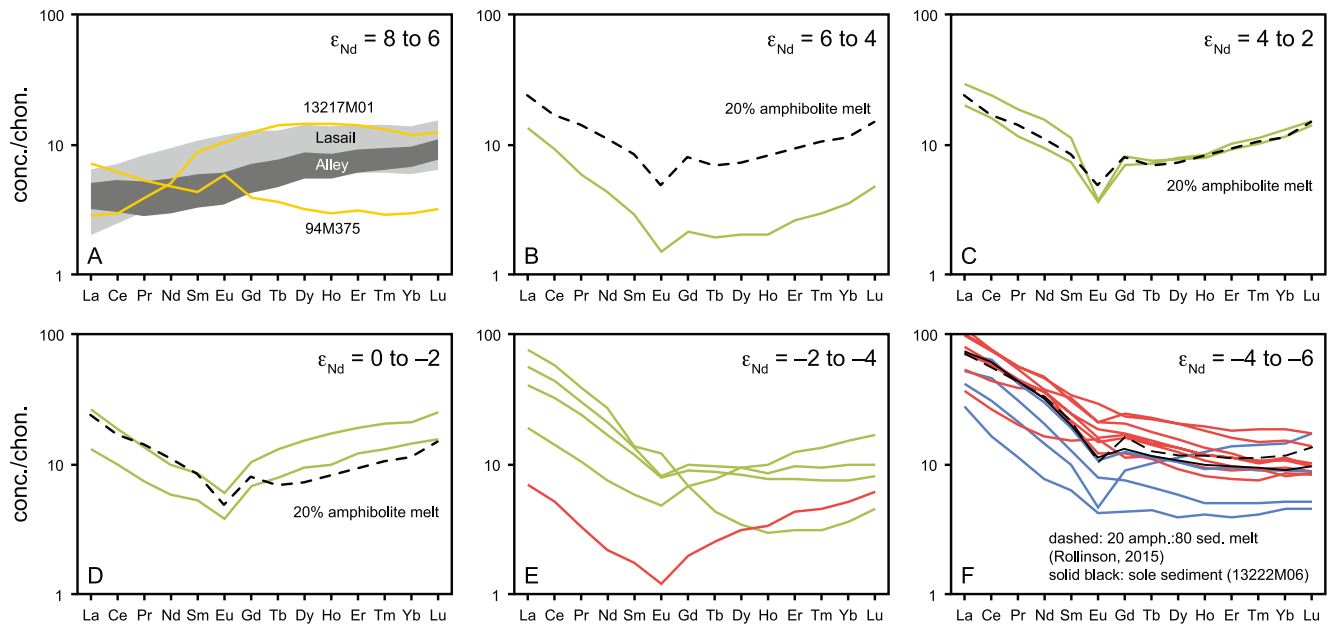


Figure 6. Rare-earth element (REE) plots for felsic dikes that intrude the mantle and lowermost crust in Oman. The data are divided based on whole rock ϵ_{Nd} , with plot colors corresponding to the color scheme in Figure 5. REE patterns from the Lasail and Alley components of the V2 series are included in (a) for comparison. The 20% amphibolite melt was modeled using the parameters described in Figure 8, with 0% garnet. Data sources: felsic mantle dike REE (this study; Amri et al., 2007; Haase et al., 2015); amphibolite+sediment melt model (Rollinson, 2015); Lasail and Alley REE patterns (Godard et al., 2003; Godard et al., 2006). Data are normalized to Anders and Grevesse (1989) multiplied by 1.36 (Korotev, 1996). This figure only includes samples with both REE and Nd isotopic data. REE, Rare earth element.

While the blue data points likely have the greatest sediment component, one of these dikes has a V-shaped REE pattern, suggesting the REE budget was dominated by amphibolite derived melts. Amphibolites from the metamorphic sole of the ophiolite have variable $\epsilon_{Nd} = +3.9$ to $+7.1$ (Cox et al., 1999; Rioux et al., 2016), and a leucocratic pod within amphibolite from the Wadi Tayin sole locality had $\epsilon_{Nd} = -7.0$ (Rioux et al., 2013). The low ϵ_{Nd} of some amphibolites could reflect either isotopic heterogeneity of the protolith basalt, or more likely, incorporation of a significant sedimentary component into the amphibolites. The low $\epsilon_{Nd}(t)$ dike with a V-shaped REE pattern may therefore include a large component of melt derived from low $\epsilon_{Nd}(t)$ amphibolite. Alternately, the V-shaped pattern could reflect variable REE patterns from sediment melts; however, we consider this to be less likely, given that most of the low ϵ_{Nd} dikes (i.e., sediment-rich) have LREE enriched patterns (Figure 6f, red and blue). In addition, while sediment derived Himalayan leucogranites do show a range of REE patterns (Guo & Wilson, 2012), it is notable that they do not include the type of V-shaped patterns observed in the Samail ophiolite.

Two final dikes have low MgO and high $\epsilon_{Nd}(t) = +7.4$ – 7.8 (yellow symbols), overlapping the range of $\epsilon_{Nd}(t)$ observed within the V1 and V2 magmatic series that form the ophiolite crust (Figure 5a). These dikes plot at the intersection of the amphibolite melting trend (green symbols) described above, and the differentiation trends for the V1 and V2 magmatic series. One of these dikes (13217M01; $\epsilon_{Nd}(t) = +7.4$) from just below the crust-mantle transition in the Sarami massif has an LREE depleted REE pattern, which is distinct from the U-shaped REE patterns of the amphibolite melting trend, but similar to the REE patterns of the V2 volcanic series (labeled sample in Figures 4a, 4c, and 6a; higher MgO yellow data point in Figure 5). This dike has a similar incompatible trace element signature to the V2 lavas, including Nb, Ta, and Th depletions and Pb and Sr peaks (Figure 4a). We therefore consider it most likely that this felsic dike formed by extensive differentiation of magmas related to the V2 series within the uppermost mantle. Interestingly, there is an offset in dates between the LREE depleted dike (13217M01) and the four dated LREE enriched mantle dikes (Rioux et al., 2021); the LREE depleted dike yielded a weighted mean $^{206}\text{Pb}/^{238}\text{U}$ date of 95.478 ± 0.032 Ma, compared to younger $^{206}\text{Pb}/^{238}\text{U}$ dates of 95.201 ± 0.032 to 94.95 ± 0.10 Ma for the other mantle dikes. The older date overlaps with the timing of crustal plutonic

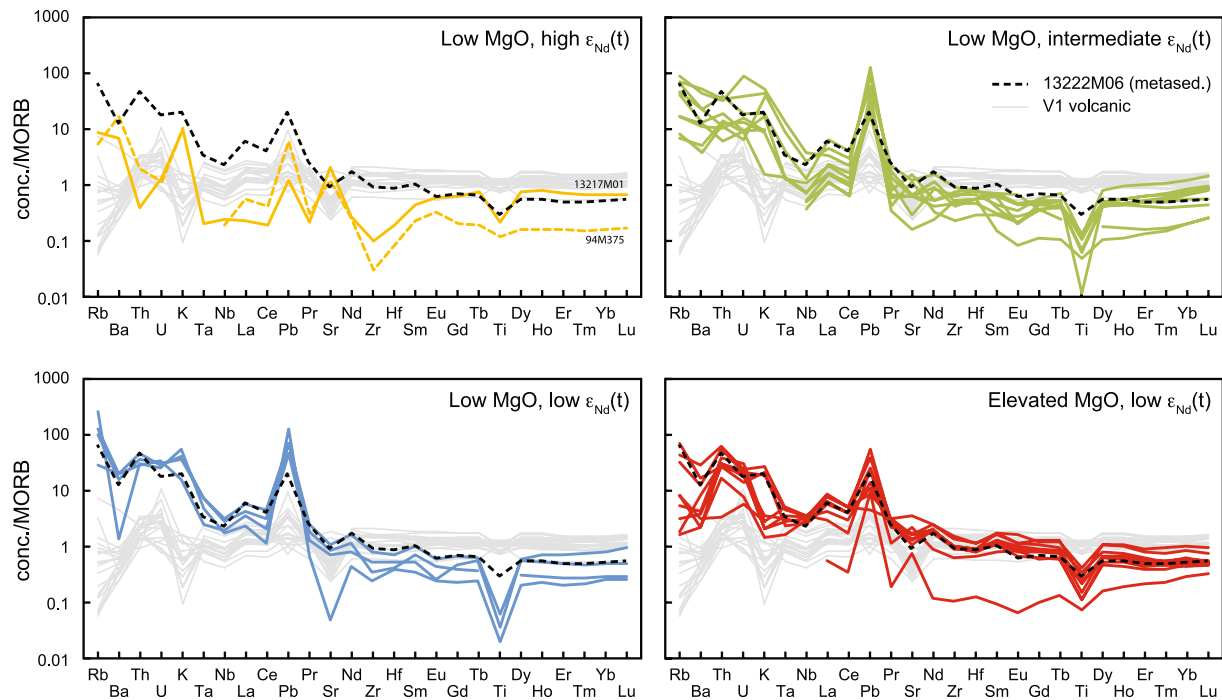


Figure 7. Extended trace element diagrams for felsic dikes that intrude the mantle and lowermost crust in Oman. Data are grouped following the trends defined in Figure 5. V1 lavas (Godard et al., 2003; Godard et al., 2006) and the composition of a sole metasediment (13222M06) are shown for comparison. Normalized to normal mid-ocean ridge basalt (Hofmann, 1988).

rocks related to V2 magmatism (Rioux et al., 2021). The data, therefore, suggest two distinct generations of felsic mantle intrusions, with an earlier set related to V2 magmatism and a later series linked to melting of underthrust amphibolite and metasediment.

In contrast, the second high $\epsilon_{Nd}(t)$ dike (94M375; $\epsilon_{Nd}(t) = +7.8$) was sampled just above the crust-mantle transition in the Samail massif, and has a slightly enriched LREE and relatively flat HREE pattern (labeled sample in Figures 4c and 6a; lower MgO yellow data point in Figure 5) (Amri et al., 2007). Rioux et al. (2013) studied an intrusion from the same swarm ~ 100 m from this sample, which yielded $\epsilon_{Nd}(t) = +6.9$ and a $^{206}\text{Pb}/^{238}\text{U}$ date of 95.063 ± 0.062 Ma (9127M01), but we do not have trace element data for the dated sample. The age of sample 9127M01 overlaps with the timing of the low $\epsilon_{Nd}(t)$ mantle dikes and is distinctly younger than the age of the potentially V2 related intrusion discussed in the preceding paragraph. We therefore hypothesize that samples 94M375 and 9127M01, which have $\epsilon_{Nd} = +6.9$ – 7.8 , represent a high ϵ_{Nd} end member of primarily amphibolite melts. The major element data from 94M375 plot within the amphibolite melt field on the Patiño Douce (1999) major element discrimination diagram, consistent with this hypothesis; however, the REE data for 94M375 lack the U-shape pattern associated with amphibolite melting. This could be due to differentiation or a different, more amphibole-poor or garnet-rich source composition. We note that the sample has an extreme Zr depletion (lowest Zr trough in Figures 4c) and a positive Eu anomaly, which could reflect zircon fractionation and plagioclase accumulation; however, simple geochemical models of these processes do not reproduce the observed REE pattern. Direct measurements of the REE in plagioclase, zircon and other trace minerals in the sample are required to more robustly test whether the observed REE pattern is related to differentiation or a different source lithology (e.g., more modal garnet).

The distinct melting and fractionation trends are best defined by major element, minor element, and REE trends; however, incompatible trace element ratios provide additional insight into the source compositions and melting processes. The analyzed sole metasediment (13222M06) has a composition similar to Global Subducting Sediment (GLOSS) (Plank & Langmuir, 1998) and is enriched in Rb, Ba, Th, U, Nb, Ta, Pb, and the LREE relative to V1 volcanic compositions (Figures 4 and 7), providing constraints on the

possible composition of the metasediment end member. Whole rock trace element compositions of sole amphibolites are intermediate between V1 and metasediment compositions, with variable enrichments in Rb, Ba, Pb, and Nb, which have been attributed to addition of these elements by slab fluids (Ishikawa et al., 2005); U and Th data were not published for the sole amphibolites. The more amphibolite-rich dikes in the Samail ophiolite are characterized by lower Th and U concentrations (Figure 7), as expected given the large compositional differences between likely sediment and amphibolite protoliths. The low Th of the amphibolite-rich melts leads to a general trend of decreasing Th/Yb with increasing amphibolite component (Figure 5g).

Previous work has also demonstrated that amphibolite melts are generally characterized by elevated Zr/Sm and low Nb/Ta (Foley et al., 2002). The inferred amphibolite-rich dikes (green data points) show a broad trend to higher Zr/Sm (Figure 5h), consistent with this observation; scatter in the trend likely reflects heterogeneity in the slab sediment composition. The low Zr/Sm of the non-V2 related high ϵ_{Nd} dike (yellow plot symbol), which we argue has the lowest sediment contribution, is likely related to zircon fractionation, as discussed above. While Foley et al. (2002) also used Nb/Ta to fingerprint amphibolite versus eclogite melting, this is a poor discriminant between amphibolite and lower pressure metasediment melts, as the range of sediment derived leucogranites from the Himalaya (Guo & Wilson, 2012) overlap the predicted range of Nb/Ta of amphibolite melts and no clear trend is seen in the felsic dike data.

Finally, sediment-derived Himalayan leucogranites are characterized by low Ce/Pb (<2) (Guo & Wilson, 2012) and the analyzed sole metasediment has a lower Ce/Pb (Ce/Pb = 5.2) than most sole amphibolites (Ce/Yb = 3.5–43.3) (Ishikawa et al., 2005) and V1 volcanic rocks (3.0–83.2) (Godard et al., 2003, 2006), suggesting this may be a useful ratio to discriminate between amphibolite and metasedimentary sources within the mantle dikes. However, there is no systematic offset in Ce/Pb between sediment-rich and amphibolite-rich dikes (Figure 5i; Ce/Pb overlap for blue and green plot symbols). This may reflect Pb addition in a fluid phase during amphibolite melting, although this is ambiguous as we do not observe a clear trend to lower Th/U (fluid immobile/fluid mobile) for amphibolite-rich dikes and Ishikawa et al. (2005) found only limited Pb enrichment from slab fluids in sole amphibolites.

In summary, our analyses suggest the felsic dikes that intrude the upper mantle and lowermost crust along the length of the ophiolite formed as a result of three distinct fractionation and mixing processes: (1) dikes with low MgO (<1 wt. %), low Ni, high SiO₂, and $\epsilon_{\text{Nd}} = -6$ to $+4$ (green and blue symbols) likely represent two component mixing between partial melts from amphibolite- to granulite-facies metasedimentary and meta-basaltic sources that were underthrust or subducted below the ophiolite, with an increasing component of metabasaltic melts at higher ϵ_{Nd} ; (2) dikes with low $\epsilon_{\text{Nd}} = -6$ to -4 , but higher MgO (>1 wt. %), higher Ni, and lower SiO₂ (red symbols) likely reflect mixing between combined meta-basaltic/meta-sedimentary melts and a mantle component consisting of either mantle derived basalts (Haase et al., 2015) or reaction with mantle harzburgite (Rollinson, 2015); and (3) a single dike with low MgO, high $\epsilon_{\text{Nd}} = +7.4$ and an LREE depleted rare earth element pattern may have formed by extensive differentiation of V2 magmas within the upper mantle.

6.2. Origin of the Felsic Mantle Dikes in the UAE Portion of the Ophiolite

The felsic dikes within the mantle section in the UAE are ~0.9–4.0 Ma younger than the similar intrusions within the Oman section (Rioux et al., 2021). Cox et al. (1999) used isotopic and geochemical data to argue that the UAE dikes range from pure metasediment partial melts to mixtures of metasediment and meta-basaltic partial melts. Rollinson (2015) grouped the Oman and UAE dikes together in deriving his three-component mixing model. The plots presented herein are generally consistent with the conclusions of Cox et al. (1999); most of the UAE dikes from Ra's Dadnah, Ra's Dibba, Wadi Hulw bin Sulayman, and Wadi Zikt plot along the amphibolite mixing trend, suggesting they represent a mix of metasedimentary and metabasaltic melts formed at amphibolite- to granulite-facies (Figure 5). A single dike analyzed by Cox et al. (1999) from the center of the Ra's Dadnah composite intrusion plots along the mantle mixing trend, consistent with assimilation of orthopyroxene and amphibole from mantle harzburgites (Rollinson, 2015) or mixing with mantle derived basalt (Haase et al., 2015). These data suggest that, although there are significant age differences, the UAE felsic dikes broadly record the same melting, mixing, and fractionation processes as the Oman dikes.

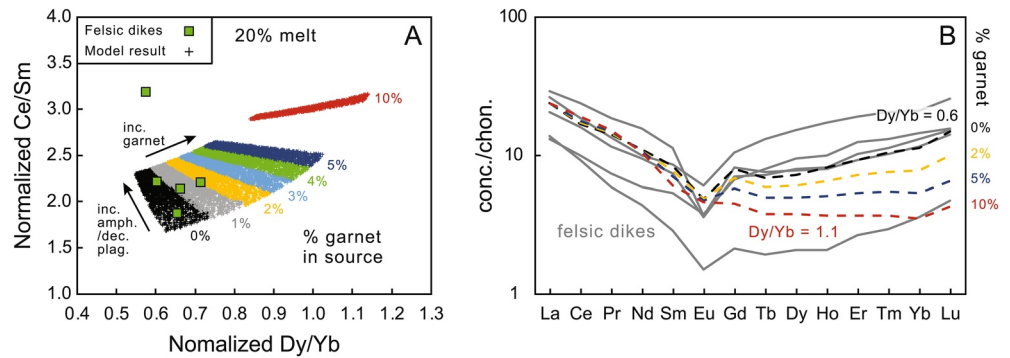


Figure 8. (a) Monte Carlo simulations of batch partial melting of an amphibolite source with 0–10 wt. % garnet ($n = 2,000$ iterations per garnet step), compared to data from low MgO, $\epsilon_{Nd}(t) > -2$, felsic mantle dikes with U- to V-shaped REE (green squares in Figure 5). Proportions of amphibole, plagioclase, and clinopyroxene were varied, as described in the text—this model has 0% titanite. The model is for 20% batch modal melting of an average V1 composition (Geotimes from Wadi Salahi) (Godard et al., 2006), using the distribution coefficients from Rollinson (2015). Inc. amph./dec. plag., increasing wt. % amphibole and decreasing wt. % plagioclase; inc. garnet, increasing wt. % garnet. (b) Model results showing the impact of 0, 2, 5, and 10 wt. % garnet in the source, compared to the REE patterns of the felsic mantle dikes (gray lines; $\epsilon_{Nd}(t) > -2$). The plotted REE patterns are for 20% batch modal melting of an amphibolite source with ~25 wt. % amphibole, ~60 wt.% plagioclase, and 15 wt. % clinopyroxene. Data are normalized to Anders and Grevesse (1989) multiplied by 1.36 (Korotev, 1996). REE, Rare earth element.

6.3. Depth of Melting

An important observation made by both Haase et al. (2015) and Rollinson (2015) is that the lack of HREE depletion in most of the felsic mantle dikes requires limited garnet in their source rocks, which constrains the depth of melting. To further quantify the amount of garnet permitted in the source of the felsic mantle dikes, we developed both traditional and Monte Carlo modal batch melting models (Rollinson, 2014b). We focused on the dikes with U- to V-shaped REE patterns, which we attribute to partial melting of an amphibolite source. In the Monte Carlo simulation, we varied the weight percent amphibole (15–60%), clinopyroxene (0–25%), garnet (0–10%), titanite (0–5%), and plagioclase (0–85%; set by difference) in an amphibolite source, and calculated the trace element composition of equilibrium partial melts. In this modeling, we did not seek to determine the exact mineralogy of the amphibolite source but instead to explore a range of realistic mineralogies. For comparison, pseudosection modeling of source mineralogies using the Gibbs free energy minimization software *Perple_X* (Connolly, 2005) (see below) suggests modal mineralogies of 30–50 wt. % amphibole, 20–50 wt. % plagioclase, and 10%–20% clinopyroxene for amphibolites at solidus temperatures and appropriate pressures for 0–10 wt. % garnet. We used source REE patterns based on the composition of amphibolite samples from the metamorphic sole (Ishikawa et al., 2005) or V1 volcanic rocks (Godard et al., 2006), which are considered the most likely analogs for the composition of the subducted slab (Supplemental Text S1).

Figure 8 shows our preferred model using the partition coefficients of Rollinson (2015), based on data from Sisson (amphibole; 1994), Bacon and Druitt (amphibole; 1988), and Rubatto and Hermann (garnet; 2007); the selected partition coefficients are from felsic systems to be consistent with the felsic composition of amphibolite partial melts (Beard & Lofgren, 1991; Rapp et al., 1991). The HREE slope of the modeled melts reflect a balance between amphibole and garnet partitioning, where amphibole in the source leads to more positive HREE slopes (i.e., lower Dy/Yb and U- to V-shaped REE patterns), while higher modal garnet decreases the HREE slope (i.e., higher Dy/Yb). Our Monte Carlo models indicate that source rocks with >5 wt. % garnet lead to flatter HREE slopes (higher Dy/Yb) than observed in the dikes (Figure 8; average V1 starting composition); the dike data are most consistent with models of ≤ 2 wt. % garnet. These results are insensitive to the percent melting.

In reality, even the dikes with U- to V-shaped REE patterns likely incorporated some sediment melt, as indicated by the variable $\epsilon_{Nd}(t)$. Sediment melts are expected to have flat to HREE depleted REE patterns (this study; Guo & Wilson, 2012; Rollinson, 2015), and the addition of a sediment melt would further reduce the predicted percentage of garnet in the amphibolite source. Given that we sought to determine the

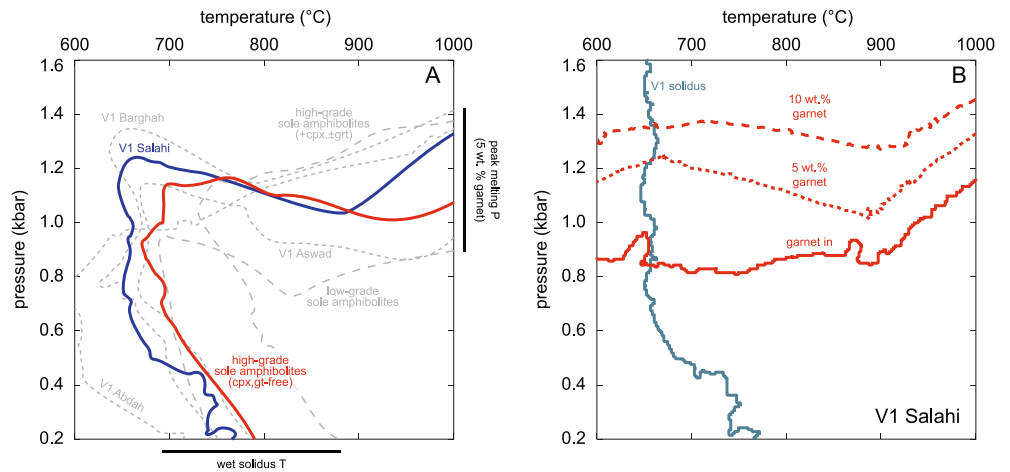


Figure 9. (a) Calculated bounds on high- $\epsilon_{\text{Nd}}(t)$ dike generation from Perple_X (Connolly, 2005). Each line represents constraints from a single bulk composition, with the low- T (near vertical) bound representing the H_2O -saturated solidus and the high- P (near horizontal) bound representing the 5 wt.% garnet modal isopleth (i.e., viable source conditions are on the high- T , low- P side of each line). The average V1 Salah and sole amphibolite compositions used in our geochemical modeling are highlighted. All lines were smoothed for clarity. (b) P - T conditions of the wet solidus and garnet isopleths for the average V1 Salah composition.

maximum percent garnet that may have existed within the amphibolite source for the felsic mantle dikes, and including sediment melts is most likely to reduce the predicted percentage of garnet in the source, we did not focus on the proportion or composition of sediment melts in the Monte Carlo models. It is possible that some of the low $\epsilon_{\text{Nd}}(t)$ samples that are LREE enriched with flat HREE (Figure 6f) could reflect melting of a garnet-rich amphibolite source (i.e., the flat HREE are a balance between the elevated HREE from the source amphibolite and HREE depletion due to a strong garnet signature); however, given the low $\epsilon_{\text{Nd}}(t)$ of these samples, we consider it more likely that the REE patterns reflect a large sediment component, as previously suggested (Haase et al., 2015; Rollinson, 2015; Spencer et al., 2017).

The extended trace element patterns of our melting models are generally consistent with the sample data, with the exceptions of the absence of negative Ti anomalies, smaller positive Pb anomalies, higher Zr and Hf concentrations, and lower Rb and Ba concentrations in the model results (Supplemental Figure S2). The higher Zr, Hf, and Ti in the model data likely reflect residual zircon, ilmenite, and/or titanite in the source (Rollinson, 2015), the low Rb and Ba are due to depletions of these elements in the selected source composition and the higher Pb observed in the samples may reflect contributions from a sediment or fluid component. In terms of the HREE slope, any residual zircon in the source would flatten the HREE and further limited the predicted modal percent garnet.

To test the sensitivity of the model results to the assumed source composition and the presence of titanite in the source, we modeled melting of a range of V1 and sole compositions and ran models containing 0–5 wt. % titanite. Given that partition coefficients (K_d) can be sensitive to mineral composition, melt composition, P , and T , we further tested our models using a range of published coefficients for amphibole, clinopyroxene, garnet, and titanite. The results of these additional models are discussed in the Supplemental Text S1 and plotted in Supplemental Figures S3–S8, and further support the conclusion that the amphibolite source for the felsic mantle dikes likely contained <5 wt. % garnet.

The relative percentage of amphibole and plagioclase in the best-fit models is somewhat dependent on the source composition. Either of the average compositions we focused on (average Salah V1 or clinopyroxene free, high-grade amphibolites) can reproduce four of the five data points from the felsic mantle dikes, but the best fit models, especially for the sole amphibolite starting composition, have less amphibole (10–40 wt. %) and more plagioclase (30–90 wt. %) than the predicted amphibolite mineralogy at the appropriate P - T based on pseudosection modeling. However, the apparent “excess” plagioclase in the source may actually reflect fractional crystallization of plagioclase from the melts (i.e., we are modeling the dike REE

based on melting alone, but their chemistry likely reflects a combination of source melting and subsequent fractional crystallization). As such, we do not expect the relative proportions of amphibole and plagioclase to necessarily match the mineralogy of the source amphibolite. The amount of plagioclase in the source (or removed during fractional crystallization) primarily changes the LREE slope (i.e., Ce/Sm) and does not significantly impact the HREE slope, and therefore does not impact the predicted percent garnet in the source.

Overall, our modeling suggests that the REE patterns of the felsic mantle dikes are most consistent with <5 wt. % garnet in the amphibolite source. To understand pressure and temperature bounds for felsic dike generation that are consistent with this result, we performed thermodynamic modeling using the Gibbs free-energy minimization software *Perple_X* v. 6.8.4 (Connolly, 2005) (Supplemental Text S1). These efforts were applied to seven subdivisions of the potential source compositions outlined above.

Based on the melt partitioning results, the source conditions for the high- ϵ_{Nd} dikes with U- to V-shaped HREE patterns are bounded by the wet solidus (at low T) and the occurrence of the 5 wt. % garnet modal isopleth (at high P); these are combined and displayed for each of the modeled bulk compositions in Figure 9. Most of the possible source rocks exhibit solidus temperatures between 700–800°C, and maximum pressures for 5 wt. % garnet between 1.0–1.4 GPa, but there are clear differences between different bulk compositions. For example, models using the bulk composition of the highest-grade, garnet-bearing sole amphibolites have a distinctly higher- T solidus (potentially reflecting prior melt extraction and significant Ca enrichments relative to other starting compositions), whereas models using the composition of the lowest-grade, garnet-free sole amphibolites exhibit far more garnet over the investigated P - T range than any other composition (reflecting higher bulk-rock FeO and MnO contents). Overall, the pseudosection results are consistent with high- ϵ_{Nd} dike generation by wet melting at $P \leq 1.4$ GPa and $T \geq 700$ –750°C, which broadly matches the P - T conditions recorded by sole amphibolites (Cowan et al., 2014; Searle & Cox, 2002; Soret et al., 2017).

7. Conclusions

The origin of felsic intrusions into the upper mantle and lower crust of the Samail ophiolite have been the focus of several recent studies. Here we build on these contributions by presenting an integrated data set of whole rock major element, trace element and Nd isotopic data from intrusions from a wider geographic area. The new and published data suggest three distinct mixing and fractionation trends. Most of the intrusions in Oman formed primarily by mixing between amphibolite and metasediment melts, with little mantle contribution. In contrast, the well-studied dike swarm at Wadi Hajr and Wadi Hemli in the southern Haylayn massif formed through three-component mixing between amphibolite-metasediment melts and a mantle component, consistent with prior research (Haase et al., 2015; Rollinson, 2014a, 2015). Finally, a single sample with high ϵ_{Nd} and an LREE-depleted trace element signature likely formed by differentiation of depleted, mantle derived magmas related to the V2 magmatic series. U-Pb zircon dates from the Oman dikes show that the V2-related dike intruded earlier, at 95.478 ± 0.032 Ma, while the rest of the dated dikes have near synchronous, younger dates of 95.201 ± 0.032 Ma to 94.95 ± 0.10 along the length of the ophiolite in Oman (Rioux et al., 2021). Combined geochemical and pseudosection modeling suggests that the dikes were generated by partial melting of underthrust material at $P \leq 1.4$ GPa and $T \geq 700$ –750°C. The distinct mixing trends of the dikes may reflect heterogeneities in thermal conditions within the mantle wedge and/or at the top of the underthrust or subducted slab and heterogeneities in the proportion of amphibolites and metasediments along any given portion of the underthrust plate. Felsic intrusions into the mantle in the UAE follow similar mixing trends to the Oman samples, with most reflecting primarily two-component mixing between amphibolite and metasediment melts, consistent with the conclusions of Cox et al. (1999); however, U-Pb dates from the felsic dikes intruding the northern termination of the ophiolite in the UAE range from 94.119 ± 0.057 to 90.998 ± 0.052 Ma (Rioux et al., 2021), indicating that felsic magmatism there significantly post-dated all other magmatic events (both mafic and felsic) recorded in the bulk of the ophiolite.

Data Availability Statement

Geochemical data from this study are available on the EarthChem Library using the following links: Table 2 major- and trace-element data: <https://doi.org/10.26022/IEDA/111896>; Table 2 isotopic data: <https://doi.org/10.26022/IEDA/111897>; Table 3 major- and trace-element data: <https://doi.org/10.26022/IEDA/111894>; Table 3 isotopic data: <https://doi.org/10.26022/IEDA/111895>.

Acknowledgments

This research was supported by United States National Science Foundation grants EAR-1250522 and 1650407 to Matthew Rioux. The authors thank the Public Authority for Mining for their support of our research in the Sultanate of Oman, and Mohammed Ali and Aisha Al Suwaidi at Khalifa University for their contributions to our work in the United Arab Emirates. The authors are grateful for insightful reviews by Karsten Haase, an anonymous reviewer, and Editor Steve Parman, which substantially improved this manuscript. Joshua Garber acknowledges support from National Science Foundation grant OISE-1545903 and The Pennsylvania State University.

References

- Adachi, Y., & Miyashita, S. (2003). Geology and petrology of the plutonic complexes in the Wadi Fizh area: Multiple magmatic events and segment structure in the northern Oman ophiolite. *Geochemistry, Geophysics, Geosystems*, 4(9), 8619. <https://doi.org/10.1029/2001gc000272>
- Alabaster, T., Pearce, J. A., & Malpas, J. (1982). The volcanic stratigraphy and petrogenesis of the Oman ophiolite complex. *Contributions to Mineralogy and Petrology*, 81(3), 168–183. <https://doi.org/10.1007/bf00371294>
- Aldiss, D. T. (1981). Plagiogranites from the ocean crust and ophiolites. *Nature*, 289(5798), 577–578. <https://doi.org/10.1038/289577a0>
- Amri, I., Benoit, M., & Ceuleneer, G. (1996). Tectonic setting for the genesis of oceanic plagiogranites: Evidence from a paleo-spreading structure in the Oman ophiolite. *Earth and Planetary Science Letters*, 139(1–2), 177–194. [https://doi.org/10.1016/0012-821x\(95\)00233-3](https://doi.org/10.1016/0012-821x(95)00233-3)
- Amri, I., Ceuleneer, G., Benoit, M., Python, M., Puga, E., & Targuisti, K. (2007). Genesis of granitoids by interaction between mantle peridotites and hydrothermal fluids in oceanic spreading setting in the Oman ophiolite. *Geogaceta*, 42, 23–26.
- Anders, E., & Grevesse, N. (1989). Abundances of the elements: Meteoritic and solar. *Geochimica et Cosmochimica Acta*, 53(1), 197–214. [https://doi.org/10.1016/0016-7037\(89\)90286-x](https://doi.org/10.1016/0016-7037(89)90286-x)
- Aries, S., Valladon, M., Polvé, M., & Dupré, B. (2000). A routine method for oxide and hydroxide interference corrections in ICP-MS chemical analysis of environmental and geological samples. *Geostandards Newsletter*, 24(1), 19–31. <https://doi.org/10.1111/j.1751-908x.2000.tb00583.x>
- Bacon, C. R., & Druitt, T. H. (1988). Compositional evolution of the zoned calcalkaline magma chamber of Mount Mazama, Crater Lake, Oregon. *Contributions to Mineralogy and Petrology*, 98(2), 224–256. <https://doi.org/10.1007/bf00402114>
- Bailey, E. H. (1981). Geologic map of Muscat-Ibra area, Sultanate of Oman. *Journal of Geophysical Research*, 86(B4).
- Barker, F. (1979). Chapter 1 - Trondhjemite: Definition, environment and hypotheses of origin. In F. Barker (Ed.), *Developments in petrology* (pp. 1–12). Elsevier.
- Beard, J. S., & Lofgren, G. E. (1991). Dehydration melting and water-saturated melting of basaltic and andesitic greenstones and amphibolites at 1, 3, and 6.9 kb. *Journal of Petrology*, 32(2), 365–401. <https://doi.org/10.1093/ptrology/32.2.365>
- Benoit, M., Ceuleneer, G., & Polvé, M. (1999). The remelting of hydrothermally altered peridotite at mid-ocean ridges by intruding mantle diapirs. *Nature*, 402(6761), 514–518. <https://doi.org/10.1038/990073>
- Benoit, M., Polvé, M., & Ceuleneer, G. (1996). Trace element and isotopic characterization of mafic cumulates in a fossil mantle diapir (Oman ophiolite). *Chemical Geology*, 134(1–3), 199–214. [https://doi.org/10.1016/s0009-2541\(96\)00087-3](https://doi.org/10.1016/s0009-2541(96)00087-3)
- Boudier, F., Ceuleneer, G., & Nicolas, A. (1988). Shear zones, thrusts and related magmatism in the Oman ophiolite: Initiation of thrusting on an oceanic ridge. *Tectonophysics*, 151(1–4), 275–296. [https://doi.org/10.1016/0040-1951\(88\)90249-1](https://doi.org/10.1016/0040-1951(88)90249-1)
- Braun, J.-J., Viers, J., Dupré, B., Polvé, M., Ndam, J., & Muller, J.-P. (1998). Solid/Liquid ree fractionation in the lateritic system of Goyoum, East Cameroon: The implication for the present dynamics of the soil covers of the humid tropical regions. *Geochimica et Cosmochimica Acta*, 62(2), 273–299. [https://doi.org/10.1016/s0016-7037\(97\)00344-x](https://doi.org/10.1016/s0016-7037(97)00344-x)
- Briqueu, L., Mével, C., & Boudier, F. (1991). Sr, Nd and Pb isotopic constraints on the genesis of a calc-alkaline plutonic suite in the Oman mountains related to the obduction process. In Tj. Peters, A. Nicolas, & R. Coleman (Eds.), *Ophiolite genesis and evolution of the oceanic lithosphere* (pp. 517–542). Sultanate of Oman: Ministry of Petroleum and Minerals.
- Browning, P., & Smewing, J. D. (1981). Processes in magma chambers beneath spreading axes: Evidence from magmatic associations in the Oman ophiolite. *Journal of the Geological Society*, 138(3), 279–280. <https://doi.org/10.1144/gsjgs.138.3.0279>
- Ceuleneer, G., Monnereau, M., & Amri, I. (1996). Thermal structure of a fossil mantle diapir inferred from the distribution of mafic cumulates. *Nature*, 379(6561), 149–153. <https://doi.org/10.1038/379149a0>
- Coleman, R. G., & Hopson, C. A. (1981). Introduction to the Oman ophiolite special issue. *Journal of Geophysical Research*, 86(B4), 2495–2496. <https://doi.org/10.1029/jb086ib04p02495>
- Connolly, J. A. D. (2005). Computation of phase equilibria by linear programming: A tool for geodynamic modeling and its application to subduction zone decarbonation. *Earth and Planetary Science Letters*, 236(1–2), 524–541. <https://doi.org/10.1016/j.epsl.2005.04.033>
- Cowan, R. J., Searle, M. P., & Waters, D. J. (2014). Structure of the metamorphic sole to the Oman Ophiolite, Sumeini Window and Wadi Tayyin: Implications for ophiolite obduction processes. *Geological Society, London, Special Publications*, 392(1), 155–175. <https://doi.org/10.1144/sp392.8>
- Cox, J., Searle, M., & Pedersen, R. (1999). The petrogenesis of leucogranitic dykes intruding the northern Semail ophiolite, United Arab Emirates: Field relationships, geochemistry and Sr/Nd isotope systematics. *Contributions to Mineralogy and Petrology*, 137(3), 267–287. <https://doi.org/10.1007/s004100050550>
- Ernewein, M., Pflumio, C., & Whitechurch, H. (1988). The death of an accretion zone as evidenced by the magmatic history of the Semail ophiolite (Oman). *Tectonophysics*, 151(1–4), 247–274. [https://doi.org/10.1016/0040-1951\(88\)90248-x](https://doi.org/10.1016/0040-1951(88)90248-x)
- Foley, S., Tiepolo, M., & Vannucci, R. (2002). Growth of early continental crust controlled by melting of amphibolite in subduction zones. *Nature*, 417(6891), 837–840. <https://doi.org/10.1038/nature00799>
- France, L., Ildefonse, B., & Koepke, J. (2009). Interactions between magma and hydrothermal system in Oman ophiolite and in IODP Hole 1256D: Fossilization of a dynamic melt lens at fast spreading ridges. *Geochemistry, Geophysics, Geosystems*, 10, Q10019. <https://doi.org/10.1029/2009gc002652>
- Frost, B. R., Barnes, C. G., Collins, W. J., Arculus, R. J., Ellis, D. J., & Frost, C. D. (2001). A geochemical classification for granitic rocks. *Journal of Petrology*, 42(11), 2033–2048. <https://doi.org/10.1093/ptrology/42.11.2033>
- Garber, J. M., Rioux, M., Kylander-Clark, A. R. C., Hacker, B. R., Vervoort, J. D., & Searle, M. P. (2020). Petrochronology of Wadi Tayyin metamorphic sole metasediment, with implications for the thermal and tectonic evolution of the samail ophiolite (Oman/UAE). *Tectonics*, 39(12), e2020TC006135. <https://doi.org/10.1029/2020tc006135>

- Ghent, E. D., & Stout, M. Z. (1981). Metamorphism at the base of the samail ophiolite, southeastern Oman Mountains. *Journal of Geophysical Research*, 86(B4), 2557–2571. <https://doi.org/10.1029/jb086ib04p02557>
- Gnos, E. (1998). Peak metamorphic conditions of garnet amphibolites beneath the semail ophiolite: Implications for an inverted pressure gradient. *International Geology Review*, 40(4), 281–304. <https://doi.org/10.1080/00206819809465210>
- Godard, M., Bosch, D., & Einaudi, F. (2006). A MORB source for low-Ti magmatism in the semail ophiolite. *Chemical Geology*, 234(1–2), 58–78. <https://doi.org/10.1016/j.chemgeo.2006.04.005>
- Godard, M., Dautria, J. M., & Perrin, M. (2003). Geochemical variability of the Oman ophiolite lavas: Relationship with spatial distribution and paleomagnetic directions. *Geochemistry, Geophysics, Geosystems*, 4(6), 8609. <https://doi.org/10.1029/2002gc000452>
- Guo, Z., & Wilson, M. (2012). The Himalayan leucogranites: Constraints on the nature of their crustal source region and geodynamic setting. *Gondwana Research*, 22(2), 360–376. <https://doi.org/10.1016/j.gr.2011.07.027>
- Haase, K. M., Freund, S., Beier, C., Koepke, J., Erdmann, M., & Hauff, F. (2016). Constraints on the magmatic evolution of the oceanic crust from plagiogranite intrusions in the Oman ophiolite. *Contributions to Mineralogy and Petrology*, 171(5), 1–16. <https://doi.org/10.1007/s00410-016-1261-9>
- Haase, K. M., Freund, S., Koepke, J., Hauff, F., & Erdmann, M. (2015). Melts of sediments in the mantle wedge of the Oman ophiolite. *Geology*, 43(4). <https://doi.org/10.1130/G36451.1>
- Hacker, B. R., & Mosenfelder, J. L. (1996). Metamorphism and deformation along the emplacement thrust of the Samail ophiolite, Oman. *Earth and Planetary Science Letters*, 144(3–4), 435–451. [https://doi.org/10.1016/s0012-821x\(96\)00186-0](https://doi.org/10.1016/s0012-821x(96)00186-0)
- Hofmann, A. W. (1988). Chemical differentiation of the Earth: The relationship between mantle, continental crust, and oceanic crust. *Earth and Planetary Science Letters*, 90(3), 297–314. [https://doi.org/10.1016/0012-821x\(88\)90132-x](https://doi.org/10.1016/0012-821x(88)90132-x)
- Ishikawa, T., Fujisawa, S., Nagaishi, K., & Masuda, T. (2005). Trace element characteristics of the fluid liberated from amphibolite-facies slab: Inference from the metamorphic sole beneath the Oman ophiolite and implication for boninite genesis. *Earth and Planetary Science Letters*, 240(2), 355–377. <https://doi.org/10.1016/j.epsl.2005.09.049>
- Ishikawa, T., Nagaishi, K., & Umino, S. (2002). Boninitic volcanism in the Oman ophiolite: Implications for thermal condition during transition from spreading ridge to arc. *Geology*, 30(10), 899–902. [https://doi.org/10.1130/0091-7613\(2002\)030<0899:bvitoo>2.0.co;2](https://doi.org/10.1130/0091-7613(2002)030<0899:bvitoo>2.0.co;2)
- Johnson, D., Hooper, P., & Conrey, R. (1999). XRF method XRF analysis of rocks and minerals for major and trace elements on a single low dilution Li-tetraborate fused bead. *Advances in X-Ray Analysis*, 41, 843–867.
- Kelly, D. (2018). *Analysis of geological materials by low dilution fusion at the Peter Hooper geoanalytical lab*. Pullman, WA. Washington State University.
- Knaack, C., Cornelius, S., & Hooper, P. (1994). *Trace element analyses of rocks and minerals by ICP-MS*. Washington State University.
- Koepke, J. r., Feig, S. T., Snow, J., & Freise, M. (2004). Petrogenesis of oceanic plagiogranites by partial melting of gabbros: An experimental study. *Contributions to Mineralogy and Petrology*, 146(4), 414–432. <https://doi.org/10.1007/s00410-003-0511-9>
- Korotev, R. L. (1996). A self-consistent compilation of elemental concentration data for 93 geochemical reference samples. *Geostandards Newsletter*, 20(2), 217–245. <https://doi.org/10.1111/j.1751-908x.1996.tb00185.x>
- Kusano, Y., Adachi, Y., Miyashita, S., & Umino, S. (2012). Lava accretion system around mid-ocean ridges: Volcanic stratigraphy in the Wadi Fizh area, northern Oman ophiolite. *Geochemistry, Geophysics, Geosystems*, 13, Q05012. <https://doi.org/10.1029/2011gc004006>
- Kusano, Y., Hayashi, M., Adachi, Y., Umino, S., & Miyashita, S. (2014). Evolution of volcanism and magmatism during initial arc stage: Constraints on the tectonic setting of the Oman ophiolite. *Geological Society, London, Special Publications*, 392(1), 177. <https://doi.org/10.1144/sp392.9>
- Kusano, Y., Umino, S., Shinjo, R., Ikei, A., Adachi, Y., Miyashita, S., & Arai, S. (2017). Contribution of slab-derived fluid and sedimentary melt in the incipient arc magmas with development of the paleo-arc in the Oman ophiolite. *Chemical Geology*, 449, 206–225. <https://doi.org/10.1016/j.chemgeo.2016.12.012>
- Lippard, S. J., Shelton, A. W., & Gass, I. G. (1986). *The ophiolite of northern Oman* (pp. 178). London. Geological Society.
- MacLeod, C. J., Lissenberg, C. J., & Bibby, L. E. (2013). Moist MORB axial magmatism in the Oman ophiolite: The evidence against a mid-ocean ridge origin. *Geology*, 41(4), 459–462. <https://doi.org/10.1130/G33904.1>
- MacLeod, C. J., & Yaouancq, G. (2000). A fossil melt lens in the Oman ophiolite: Implications for magma chamber processes at fast spreading ridges. *Earth and Planetary Science Letters*, 176(3–4), 357–373. [https://doi.org/10.1016/s0012-821x\(00\)00020-0](https://doi.org/10.1016/s0012-821x(00)00020-0)
- Maunder, B., Prytulak, J., Goes, S., & Reagan, M. (2020). Rapid subduction initiation and magmatism in the western Pacific driven by internal vertical forces. *Nature Communications*, 11(1), 1874. <https://doi.org/10.1038/s41467-020-15737-4>
- McCulloch, M. T., Gregory, R. T., Wasserburg, G. J., & Taylor, H. P. (1981). Sm-Nd, Rb-Sr, and 180/16O isotopic systematics in an oceanic crustal section: Evidence from the Samail Ophiolite. *Journal of Geophysical Research*, 86(B4), 2721–2735. <https://doi.org/10.1029/jb086ib04p02721>
- Natland, J. H., & Dick, H. J. B. (2002). Stratigraphy and composition of gabbros drilled in Ocean drilling program hole 735B, Southwest Indian ridge; a synthesis of geochemical data. In J. H. Natland, H. J. B. Dick, D. J. Miller, & R. P. Von Herzen (Eds.), *Proceedings of the ocean drilling program, Scientific Results*, 176. College Station, TX: Ocean Drilling Program.
- Nicolas, A., Boudier, F., Ildefonse, B., & Ball, E. (2000). Accretion of Oman and United Arab Emirates ophiolite – Discussion of a new structural map. *Marine Geophysical Researches*, 21(3), 147–180. <https://doi.org/10.1023/a:1026769727917>
- Nicolas, A., Boudier, F., Koepke, J., France, L., Ildefonse, B., & Mevel, C. (2008). Root zone of the sheeted dike complex in the Oman ophiolite. *Geochemistry, Geophysics, Geosystems*, 9, Q05001. <https://doi.org/10.1029/2007gc001918>
- Nikolaeva, K., Gerya, T. V., & Connolly, J. A. D. (2008). Numerical modelling of crustal growth in intraoceanic volcanic arcs. *Physics of the Earth and Planetary Interiors*, 171(1), 336–356. <https://doi.org/10.1016/j.pepi.2008.06.026>
- Pallister, J. S., & Hopson, C. A. (1981). Samail ophiolite plutonic suite: Field relations, phase variation, cryptic variation and layering, and a model of a spreading ridge magma chamber. *Journal of Geophysical Research*, 86(B4), 2593–2644. <https://doi.org/10.1029/jb086ib04p02593>
- Patiño Douce, A. E. (1999). What do experiments tell us about the relative contributions of crust and mantle to the origin of granitic magmas? *Geological Society, London, Special Publications*, 168(1), 55–75. <https://doi.org/10.1144/gsl.sp.1999.168.01.05>
- Pearce, J. A. (1989). High T/P metamorphism and granite genesis beneath ophiolite thrust sheets. *Ophioliti*, 14(3), 195–211.
- Pearce, J. A., Alabaster, T., Shelton, A. W., & Searle, M. P. (1981). The Oman ophiolite as a cretaceous arc-basin complex: Evidence and implications. *Philosophical Transactions of the Royal Society of London – Series A: Mathematical and Physical Sciences*, 300(1454), 299–317. <https://doi.org/10.1098/rsta.1981.0066>
- Peters, T., & Kamber, B. S. (1994). Peraluminous potassium-rich granitoids in the Semail Ophiolite. *Contributions to Mineralogy and Petrology*, 118(3), 229–238. <https://doi.org/10.1007/bf00306644>

- Plank, T., & Langmuir, C. H. (1998). The chemical composition of subducting sediment and its consequences for the crust and mantle. *Chemical Geology*, 145(3–4), 325–394. [https://doi.org/10.1016/s0009-2541\(97\)00150-2](https://doi.org/10.1016/s0009-2541(97)00150-2)
- Python, M., & Ceuleneer, G. (2003). Nature and distribution of dykes and related melt migration structures in the mantle section of the Oman ophiolite. *Geochemistry, Geophysics, Geosystems*, 4(7), 8612. <https://doi.org/10.1029/2002gc000354>
- Rapp, R. P., Watson, E. B., & Miller, C. F. (1991). Partial melting of amphibolite/eclogite and the origin of Archean trondhjemites and tonalites. *Precambrian Research*, 51(1), 1–25. [https://doi.org/10.1016/0301-9268\(91\)90092-o](https://doi.org/10.1016/0301-9268(91)90092-o)
- Rioux, M., Bowring, S. A., Kelemen, P. B., Gordon, S., Dudás, F., & Miller, R. (2012). Rapid crustal accretion and magma assimilation in the Oman-U.A.E. ophiolite: High precision U-Pb zircon geochronology of the gabbroic crust. *Journal of Geophysical Research*, 117, B07201. <https://doi.org/10.1029/2012jb009273>
- Rioux, M., Bowring, S., Kelemen, P., Gordon, S., Miller, R., & Dudás, F. (2013). Tectonic development of the Samail ophiolite: High-precision U-Pb zircon geochronology and Sm-Nd isotopic constraints on crustal growth and emplacement. *Journal of Geophysical Research: Solid Earth and Planets*, 118(5), 2085–2101. <https://doi.org/10.1002/jgrb.50139>
- Rioux, M., Garber, J., Bauer, A., Bowring, S., Searle, M., Kelemen, P., & Hacker, B. (2016). Synchronous formation of the metamorphic sole and igneous crust of the Semail ophiolite: New constraints on the tectonic evolution during ophiolite formation from high-precision U-Pb zircon geochronology. *Earth and Planetary Science Letters*, 451, 708–195. <https://doi.org/10.1016/j.epsl.2016.06.051>
- Rioux, M., Garber, J. M., Searle, M., Kelemen, P., Miyashita, S., Adachi, Y., & Bowring, S. (2021). High-precision U-Pb zircon dating of late magmatism in the Semail ophiolite: A record of subduction initiation. *Journal of Geophysical Research: Solid Earth*, 126, e2020JB020758. <https://doi.org/10.1029/2020JB020758>
- Rollinson, H. (2009). New models for the genesis of plagiogranites in the Oman ophiolite. *Lithos*, 112(3–4), 603–614. <https://doi.org/10.1016/j.lithos.2009.06.006>
- Rollinson, H. (2014). Plagiogranites from the mantle section of the Oman ophiolite: Models for early crustal evolution. *Geological Society, London, Special Publications*, 392(1), 247–261. <https://doi.org/10.1144/sp392.13>
- Rollinson, H. (2015). Slab and sediment melting during subduction initiation: Granitoid dykes from the mantle section of the Oman ophiolite. *Contributions to Mineralogy and Petrology*, 170(3), 1–20. <https://doi.org/10.1007/s00410-015-1177-9>
- Rollinson, H. R. (2014). *Using geochemical data: Evaluation, presentation, interpretation*. Routledge.
- Rubatto, D., & Hermann, J. (2007). Experimental zircon/melt and zircon/garnet trace element partitioning and implications for the geochronology of crustal rocks. *Chemical Geology*, 241(1), 38–61. <https://doi.org/10.1016/j.chemgeo.2007.01.027>
- Rushmer, T. (1991). Partial melting of two amphibolites: Contrasting experimental results under fluid-absent conditions. *Contributions to Mineralogy and Petrology*, 107(1), 41–59. <https://doi.org/10.1007/bf00311184>
- Searle, M. P. (1985). Sequence of thrusting and origin of culminations in the northern and central Oman mountains. *Journal of Structural Geology*, 7(2), 129–143. [https://doi.org/10.1016/0191-8141\(85\)90127-0](https://doi.org/10.1016/0191-8141(85)90127-0)
- Searle, M. P., & Cox, J. (2002). Subduction zone metamorphism during formation and emplacement of the Semail ophiolite in the Oman mountains. *Geological Magazine*, 139(3), 241–255. <https://doi.org/10.1017/s0016756802006532>
- Searle, M. P., Lippard, S. J., Smewing, J. D., & Rex, D. C. (1980). Volcanic rocks beneath the Semail ophiolite nappe in the northern Oman mountains and their significance in the mesozoic evolution of Tethys. *Journal of the Geological Society*, 137(5), 589–604. <https://doi.org/10.1144/gsjgs.137.5.0589>
- Searle, M. P., & Malpas, J. (1980). Structure and metamorphism of rocks beneath the Semail ophiolite of Oman and their significance in ophiolite obduction. *Transactions of the Royal Society of Edinburgh: Earth Sciences*, 71, 247–262. <https://doi.org/10.1017/s0263593300013614>
- Searle, M. P., & Malpas, J. (1982). Petrochemistry and origin of sub-ophiolitic metamorphic and related rocks in the Oman mountains. *Journal of the Geological Society*, 139(3), 235–248. <https://doi.org/10.1144/gsjgs.139.3.0235>
- Searle, M. P., Waters, D. J., Garber, J. M., Rioux, M., Cherry, A. G., & Ambrose, T. K. (2015). Structure and metamorphism beneath the obducting Oman ophiolite: Evidence from the Bani Hamid granulites, northern Oman mountains. *Geosphere*, 11(6), 1812–1836. <https://doi.org/10.1130/GES01199.1>
- Sisson, T. W. (1994). Hornblende-melt trace-element partitioning measured by ion microprobe. *Chemical Geology*, 117(1), 331–344. [https://doi.org/10.1016/0009-2541\(94\)90135-x](https://doi.org/10.1016/0009-2541(94)90135-x)
- Soret, M., Agard, P., Dubacq, B., Plunder, A., & Yamato, P. (2017). Petrological evidence for stepwise accretion of metamorphic soles during subduction infancy (Semail ophiolite, Oman and UAE). *Journal of Metamorphic Geology*, 35(9), 1051–1080. <https://doi.org/10.1111/jmg.12267>
- Spencer, C. J., Cavosie, A. J., Raub, T. D., Rollinson, H., Jeon, H., Searle, M. P., et al. (2017). Evidence for melting mud in Earth's mantle from extreme oxygen isotope signatures in zircon. *Geology*, 45(11), 975–978. <https://doi.org/10.1130/g39402.1>
- Steenberg, L., Boroughs, S., & Knaack, C. (2017). Estimation of accuracy and precision for trace elements analyzed by inductively coupled plasma mass spectrometry (ICP-MS) at the Peter Hooper Geoanalytical Laboratory, Washington State University. In *Geological society of America annual meeting*. Seattle, Washington. Geological Society of America Abstracts with Programs.
- Tsuchiya, N., Shibata, T., Yoshikawa, M., Adachi, Y., Miyashita, S., Adachi, T., et al. (2013). Petrology of Lasail plutonic complex, northern Oman ophiolite, Oman: An example of arc-like magmatism associated with ophiolite detachment. *Lithos*, 156–159, 120–138. <https://doi.org/10.1016/j.lithos.2012.10.013>
- Usui, Y., & Yamazaki, S. (2010). Salvaging primary remanence from hydrothermally altered oceanic gabbros in the Oman ophiolite: A selective destructive demagnetization approach. *Physics of the Earth and Planetary Interiors*, 181(1–2), 1–11. <https://doi.org/10.1016/j.pepi.2010.04.008>
- Wilson, D. S., Teagle, D. A. H., Alt, J. C., & Banerjee, N. R. (2006). Drilling to gabbro in intact ocean crust. *Science*, 312(5776), 1016. <https://doi.org/10.1126/science.1126090>
- Zhang, C., Holtz, F., Koepke, J., Wolff, P. E., Ma, C., & Bédard, J. H. (2013). Constraints from experimental melting of amphibolite on the depth of formation of garnet-rich restites, and implications for models of Early Archean crustal growth. *Precambrian Research*, 231, 206–217. <https://doi.org/10.1016/j.precamres.2013.03.004>

References From the Supporting Information

- Adam, J., & Green, T. H. (1994). The effects of pressure and temperature on the partitioning of Ti, Sr and REE between amphibole, clinopyroxene and basaltic melts. *Chemical Geology*, 117(1), 219–233. [https://doi.org/10.1016/0009-2541\(94\)90129-5](https://doi.org/10.1016/0009-2541(94)90129-5)

- Adam, J., Green, T. H., & Sie, S. H. (1993). Proton microprobe determined partitioning of Rb, Sr, Ba, Y, Zr, Nb and Ta between experimentally produced amphiboles and silicate melts with variable F content. *Chemical Geology*, *109*(1), 29–49. [https://doi.org/10.1016/0009-2541\(93\)90060-v](https://doi.org/10.1016/0009-2541(93)90060-v)
- Bachmann, O., Dungan, M. A., & Bussy, F. (2005). Insights into shallow magmatic processes in large silicic magma bodies: The trace element record in the Fish Canyon magma body, Colorado. *Contributions to Mineralogy and Petrology*, *149*(3), 338–349. <https://doi.org/10.1007/s00410-005-0653-z>
- Bédard, J. H. (2014). Parameterizations of calcic clinopyroxene-melt trace element partition coefficients. *Geochemistry, Geophysics, Geosystems*, *15*(2), 303–336. <https://doi.org/10.1002/2013gc005112>
- Brenan, J. M., Shaw, H. F., Ryerson, F. J., & Phinney, D. L. (1995). Experimental determination of trace-element partitioning between pargasite and a synthetic hydrous andesitic melt. *Earth and Planetary Science Letters*, *135*(1), 1–11. [https://doi.org/10.1016/0012-821x\(95\)00139-4](https://doi.org/10.1016/0012-821x(95)00139-4)
- Dalpé, C., & Baker, D. R. (2000). Experimental investigation of large-ion-lithophile-element-, high-field-strength-element- and rare-earth-element-partitioning between calcic amphibole and basaltic melt: The effects of pressure and oxygen fugacity. *Contributions to Mineralogy and Petrology*, *140*(2), 233–250. <https://doi.org/10.1007/s004100000181>
- Fuhrman, M. L., & Lindsley, D. H. (1988). Ternary-feldspar modeling and thermometry. *American Mineralogist*, *73*(3–4), 201–215.
- Green, E. C. R., White, R. W., Diener, J. F. A., Powell, R., Holland, T. J. B., & Palin, R. M. (2016). Activity-composition relations for the calculation of partial melting equilibria in metabasic rocks. *Journal of Metamorphic Geology*, *34*(9), 845–869. <https://doi.org/10.1111/jmg.12211>
- Hilyard, M., Nielsen, R. L., Beard, J. S., Patin-Douce, A., & Blencoe, J. (2000). Experimental determination of the partitioning behavior of rare earth and high field strength elements between pargasitic amphibole and natural silicate melts. *Geochimica et Cosmochimica Acta*, *64*(6), 1103–1120. [https://doi.org/10.1016/S0016-7037\(99\)00379-8](https://doi.org/10.1016/S0016-7037(99)00379-8)
- Holland, T., & Powell, R. (1991). A Compensated-Redlich-Kwong (CORK) equation for volumes and fugacities of CO₂ and H₂O in the range 1 bar to 50 kbar and 100–1600°C. *Contributions to Mineralogy and Petrology*, *109*(2), 265–277. <https://doi.org/10.1007/bf00306484>
- Holland, T. J. B., & Powell, R. (2011). An improved and extended internally consistent thermodynamic dataset for phases of petrological interest, involving a new equation of state for solids. *Journal of Metamorphic Geology*, *29*(3), 333–383. <https://doi.org/10.1111/j.1525-1314.2010.00923.x>
- Klein, M., Stosch, H.-G., & Seck, H. A. (1997). Partitioning of high field-strength and rare-earth elements between amphibole and quartz-dioritic to tonalitic melts: An experimental study. *Chemical Geology*, *138*(3), 257–271. [https://doi.org/10.1016/S0009-2541\(97\)00019-3](https://doi.org/10.1016/S0009-2541(97)00019-3)
- Klein, M., Stosch, H.-G., Seck, H. A., & Shimizu, N. (2000). Experimental partitioning of high field strength and rare earth elements between clinopyroxene and garnet in andesitic to tonalitic systems. *Geochimica et Cosmochimica Acta*, *64*(1), 99–115. [https://doi.org/10.1016/S0016-7037\(99\)00178-7](https://doi.org/10.1016/S0016-7037(99)00178-7)
- LaTourrette, T., Hervig, R. L., & Holloway, J. R. (1995). Trace element partitioning between amphibole, phlogopite, and basanite melt. *Earth and Planetary Science Letters*, *135*(1), 13–30. [https://doi.org/10.1016/0012-821x\(95\)00146-4](https://doi.org/10.1016/0012-821x(95)00146-4)
- Mahood, G., & Hildreth, W. (1983). Large partition coefficients for trace elements in high-silica rhyolites. *Geochimica et Cosmochimica Acta*, *47*(1), 11–30. [https://doi.org/10.1016/0016-7037\(83\)90087-x](https://doi.org/10.1016/0016-7037(83)90087-x)
- Norman, M., Garcia, M. O., & Pietruszka, A. J. (2005). Trace-element distribution coefficients for pyroxenes, plagioclase, and olivine in evolved tholeiites from the 1955 eruption of Kilauea Volcano, Hawaii, and petrogenesis of differentiated rift-zone lavas. *American Mineralogist*, *90*(5–6), 888–899. <https://doi.org/10.2138/am.2005.1780>
- Olin, P. H., & Wolff, J. A. (2010). Rare earth and high field strength element partitioning between iron-rich clinopyroxenes and felsic liquids. *Contributions to Mineralogy and Petrology*, *160*(5), 761–775. <https://doi.org/10.1007/s00410-010-0506-2>
- Olin, P. H., & Wolff, J. A. (2012). Partitioning of rare earth and high field strength elements between titanite and phonolitic liquid. *Lithos*, *128–131*, 46–54. <https://doi.org/10.1016/j.lithos.2011.10.007>
- Prowatke, S., & Klemme, S. (2005). Effect of melt composition on the partitioning of trace elements between titanite and silicate melt. *Geochimica et Cosmochimica Acta*, *69*(3), 695–709. <https://doi.org/10.1016/j.gca.2004.06.037>
- Qian, Q., & Hermann, J. (2013). Partial melting of lower crust at 10–15 kbar: Constraints on adakite and TTG formation. *Contributions to Mineralogy and Petrology*, *165*(6), 1195–1224. <https://doi.org/10.1007/s00410-013-0854-9>
- Sisson, T. W. (1991). Pyroxene-high silica rhyolite trace element partition coefficients measured by ion microprobe. *Geochimica et Cosmochimica Acta*, *55*(6), 1575–1585. [https://doi.org/10.1016/0016-7037\(91\)90129-s](https://doi.org/10.1016/0016-7037(91)90129-s)
- Sisson, T. W., & Bacon, C. R. (1992). Garnet/high-silica rhyolite trace element partition coefficients measured by ion microprobe. *Geochimica et Cosmochimica Acta*, *56*(5), 2133–2136. [https://doi.org/10.1016/0016-7037\(92\)90336-h](https://doi.org/10.1016/0016-7037(92)90336-h)
- Taylor, R. J. M., Harley, S. L., Hinton, R. W., Elphick, S., Clark, C., & Kelly, N. M. (2015). Experimental determination of REE partition coefficients between zircon, garnet and melt: A key to understanding high-T crustal processes. *Journal of Metamorphic Geology*, *33*(3), 231–248. <https://doi.org/10.1111/jmg.12118>
- Tiepolo, M., Oberti, R., & Vannucci, R. (2002). Trace-element incorporation in titanite: Constraints from experimentally determined solid/liquid partition coefficients. *Chemical Geology*, *191*(1), 105–119. [https://doi.org/10.1016/S0009-2541\(02\)00151-1](https://doi.org/10.1016/S0009-2541(02)00151-1)
- Tiepolo, M., Oberti, R., Zanetti, A., Vannucci, R., & Foley, S. F. (2007). Trace-element partitioning between amphibole and silicate melt. *Reviews in Mineralogy and Geochemistry*, *67*(1), 417–452. <https://doi.org/10.2138/rmg.2007.67.11>
- Tiepolo, M., Vannucci, R., Bottazzi, P., Oberti, R., Zanetti, A., & Foley, S. (2000). Partitioning of rare Earth elements, Y, Th, U, and Pb between pargasite, kaersutite, and basanite to trachyte melts: Implications for percolated and veined mantle. *Geochemistry, Geophysics, Geosystems*, *1*(8), 1039. <https://doi.org/10.1029/2000gc000064>
- White, R. W., Powell, R., & Clarke, G. L. (2002). The interpretation of reaction textures in Fe-rich metapelitic granulites of the Musgrave Block, central Australia: Constraints from mineral equilibria calculations in the system K₂O-FeO-MgO-Al₂O₃-SiO₂-H₂O-TiO₂-Fe₂O₃. *Journal of Metamorphic Geology*, *20*(1), 41–55. <https://doi.org/10.1046/j.0263-4929.2001.00349.x>
- White, R. W., Powell, R., Holland, T. J. B., Johnson, T. E., & Green, E. C. R. (2014). New mineral activity-composition relations for thermodynamic calculations in metapelitic systems. *Journal of Metamorphic Geology*, *32*(3), 261–286. <https://doi.org/10.1111/jmg.12071>
- White, R. W., Powell, R., & Johnson, T. E. (2014). The effect of Mn on mineral stability in metapelites revisited: New a-x relations for manganese-bearing minerals. *Journal of Metamorphic Geology*, *32*(8), 809–828. <https://doi.org/10.1111/jmg.12095>